Mon. Not. R. Astron. Soc. **371,** 1057–1086 (2006) doi:10.1111/j.1365-2966.2006.10775.x

Cosmological radiative transfer codes comparison project – I. The static density field tests

Ilian T. Iliev,[1⋆] Benedetta Ciardi,[2] Marcelo A. Alvarez,[3] Antonella Maselli,[2] Andrea Ferrara,[4] Nickolay Y. Gnedin,[5,6] Garrelt Mellema,[7,8] Taishi Nakamoto,[9] Michael L. Norman,[10] Alexei O. Razoumov,[11] Erik-Jan Rijkhorst,[8] Jelle Ritzerveld,[8] Paul R. Shapiro,[3] Hajime Susa,[12] Masayuki Umemura[9] and Daniel J. Whalen[10,13]

[1]*Canadian Institute for Theoretical Astrophysics, University of Toronto, 60 St. George Street, Toronto, ON M5S 3H8, Canada*
[2]*Max-Planck-Institut für Astrophysik, 85741 Garching, Germany*
[3]*Department of Astronomy, University of Texas, Austin, TX 78712-1083, USA*
[4]*SISSA/International School for Advanced Studies, Via Beirut 4, 34014 Trieste, Italy*
[5]*Fermilab, MS209, PO 500, Batavia, IL 60510, USA*
[6]*Department of Astronomy & Astrophysics, The University of Chicago, Chicago, IL 60637, USA*
[7]*ASTRON, PO Box 1, NL-7990 AA Dwingeloo, the Netherlands*
[8]*Sterrewacht Leiden, PO Box 9513, NL-2300 RA Leiden, the Netherlands*
[9]*Center for Computational Sciences, University of Tsukuba, Tsukuba, Ibaraki 305-8577, Japan*
[10]*Center for Astrophysics and Space Sciences, University of California, San Diego, 9500 Gilman Drive, La Jolla, CA 92093-0424, USA*
[11]*Physics Division, Oak Ridge National Laboratory, Oak Ridge, TN 37831-6354, USA*
[12]*Department of Physics, College of Science, Rikkyo University, 3-34-1 Nishi-Ikebukuro, Toshimaku, Tokyo, Japan*
[13]*T-6 Theoretical Astrophysics, Los Alamos National Laboratory, Los Alamos, NM 87545, USA*

Accepted 2006 June 27. Received 2006 June 26; in original form 2006 March 7

ABSTRACT

Radiative transfer (RT) simulations are now at the forefront of numerical astrophysics. They are becoming crucial for an increasing number of astrophysical and cosmological problems; at the same time their computational cost has come within reach of currently available computational power. Further progress is retarded by the considerable number of different algorithms (including various flavours of ray tracing and moment schemes) developed, which makes the selection of the most suitable technique for a given problem a non-trivial task. Assessing the validity ranges, accuracy and performances of these schemes is the main aim of this paper, for which we have compared 11 independent RT codes on five test problems: (0) basic physics; (1) isothermal H II region expansion; (2) H II region expansion with evolving temperature; (3) I-front trapping and shadowing by a dense clump and (4) multiple sources in a cosmological density field. The outputs of these tests have been compared and differences analysed. The agreement between the various codes is satisfactory although not perfect. The main source of discrepancy appears to reside in the multifrequency treatment approach, resulting in different thicknesses of the ionized-neutral transition regions and the temperature structure. The present results and tests represent the most complete benchmark available for the development of new codes and improvement of existing ones. To further this aim all test inputs and outputs are made publicly available in digital form.

Key words: radiative transfer – ISM: bubbles – H II regions – galaxies: formation – intergalactic medium – cosmology: theory.

1 INTRODUCTION

Numerous physical problems require a detailed understanding of radiative transfer (RT) of photons in different environments, ranging from intergalactic and interstellar medium to stellar or planetary atmospheres. In particular, a number of problems of cosmological interest cannot be solved without incorporating RT calculations, e.g. modelling and understanding of the Lyα forest, absorption lines in spectra of high-z quasars, radiative feedback effects, the reionization of the intergalactic medium (IGM) and star formation, just to mention a few (see e.g. Ciardi & Ferrara 2005, for a recent review on

⋆E-mail: iliev@cita.utoronto.ca

some of these topics). In many of these situations, the physical conditions are such that the gas in which photons propagate is optically thick; also, the geometry of the problem often is quite complex. As a consequence, approaches relying on optically thin or geometrical approximations yield unsatisfactory (and sometimes incorrect) results.

The RT equation in 3D space has seven (three spatial, two angular, one frequency, one time) dimensions. Although in specific cases certain kinds of symmetry or approximations can be exploited, leading to a partial simplification, most problems of astrophysical and cosmological interest remain very complex. For this reason, although the basic physics involved is well understood, the detailed solution of the complete RT equation is presently beyond available computational capabilities. In addition, the technical implementation of the RT equation in numerical codes is a very young and immature subject in astrophysics.

RT approaches have been attempted in the past to study specific problems such as the light curves of supernovae, radiation from protostellar and active galactic nuclei accretion discs, line radiation from collapsing molecular clouds, continuum photon escape from galaxies and the effects of dust obscuration in galaxies. Typically, either the low dimensionality of these approaches or the simplified physics allowed a numerical treatment that resulted in a sufficiently low computational cost given the available machines. As this last constraint has become less demanding, the number and type of desirable applications have expanded extremely rapidly, particularly spreading to the fields of galaxy formation and cosmology.

Following this wave of excitement, several groups then attacked the problem from a variety of perspectives by using completely different, independent and dedicated numerical algorithms. It was immediately clear that the validation and assessment of the various codes were crucial in order not to waste (always) limited computational and human resources. At that point, the community faced the problem that, in contrast with e.g. gasdynamical studies, very few simple RT problems admit exact analytical solutions that could be used as benchmarks. Just a few years ago, only a few RT codes were available and these were still mostly in the testing/optimization phase, and therefore lacking the necessary degree of stability required to isolate truly scientific results from uncertainties due to internal programming bugs. In the last few years, the subject has rapidly changed. Not only has the reliability of existing codes matured, a new crop of codes based on novel techniques has been developed, making a comparison of them timely. The time is now ripe to do this comparison project in a fairly complete and meaningful form and this paper presents the detailed outcome of our effort.

This project is in a similar spirit to the well-known Santa Barbara Cluster Comparison project (Frenk et al. 1999), but we utilize a somewhat different approach from that project. Instead of considering a single, complex problem like the Santa Barbara Cluster Comparison did, we consider a set of relatively simple problems. The aim of the present comparison is to determine the type of problems the codes are (un)able to solve, to understand the origin of the differences inevitably found in the results, to stimulate improvements and further developments of the existing codes and, finally, to serve as a benchmark to testing future ones. We therefore invite interested RT researchers to make use of our results, including test descriptions, input and output data, all of which can be found in digital form at the project website http://www.mpa-garching.mpg.de/tsu3/. At this stage, our interest is not focused on the performances of the codes in terms of speed and optimization.

This project is a collaboration of a large number of cosmological RT researchers and includes a wide range of different methods (e.g. various versions of ray tracing, as well as moment schemes), some of which have already been applied to study a variety of astrophysical and cosmological problems. The comparison is made among 11 independent codes, each of which is described concisely in Section 2 (and more extensively in the corresponding methodology paper, available in most cases). We would like to emphasize that the interaction among the various participating groups has already resulted in many improvements of the participating codes.

Here, we present the results from a set of tests on fixed density fields, both homogeneous and inhomogeneous, which verify the RT methods themselves. In a follow-up paper, we plan to discuss the direct coupling to gasdynamics and compare the results on a set of several radiative hydrodynamics problems.

2 THE CODES

In this section, we briefly describe the 11 RT codes which are taking part in this comparison project. The descriptions point to the more detailed methodology papers, available in most cases. Details of the codes and their features are summarized in Table 1.

2.1 C^2-RAY: photon-conserving transport of ionizing radiation (G. Mellema, I. Iliev, P. Shapiro, M. Alvarez)

C^2-RAY is a grid-based short characteristics (e.g. Raga et al. 1999) ray-tracing code which is photon conserving and causally traces the rays away from the ionizing sources up to each cell. Explicit photon conservation is assured by taking a finite-volume approach when calculating the photoionization rates, and by using time-averaged optical depths. The latter property allows for integration time-steps

Table 1. Participating codes and their current features.

Code	Grid	Parallelization	Gasdynamics	Helium	Rec. radiation
C^2-RAY	Fixed/AMR	Shared	Yes	No	No
OTVET	Fixed	Shared	Yes	Yes	Yes
CRASH	Fixed	No	No	Yes	Yes
RSPH	No grid, particle-based	Distributed	Yes	No	No
ART	Fixed	Distributed	No	No	Yes
FTTE	Fixed/AMR	No	Yes	Yes	Yes
SIMPLEX	Unstructured	No	No	No	Yes
ZEUS-MP	Fixed	Distributed	Yes	No	No
FLASH-HC	Fixed/AMR	Distributed	Yes	No	No
IFT	Fixed/AMR	No	No	No	No
CORAL	AMR	No	Yes	Yes	No

much larger than the ionization time-scale, which leads to a considerable speed-up of the calculation and facilitates the coupling of the code to gasdynamic evolution. The code is described and tested in detail in Mellema et al. (2006a).

The frequency dependence of the photoionization rates and photoionization heating rates are dealt with by using frequency-integrated rates, stored as functions of the optical depth at the ionization threshold. In its current version, the code includes only hydrogen and does not include the effects of helium, although they could be added in a relatively straightforward way.

The transfer calculation is done using short characteristics, where the optical depth is calculated by interpolating values of grid cells lying along the line of sight (LOS) towards the source. Because of the causal nature of the ray tracing, the calculation cannot easily be parallelized through domain decomposition. However, using OPENMP the code is efficiently parallelized over the sources. The code is currently used for large-scale simulations of cosmic reionization and its observability (Iliev et al. 2006b; Mellema et al. 2006b) on grid sizes up to 406^3 and up to more than 10^5 ionizing sources.

There are 1D, 2D and 3D versions of the code available. It was developed to be directly coupled with hydrodynamics calculations. The large time-steps allowed for the RT enable the use of the hydrodynamic time-step for evolving the combined system. The first gasdynamic application of our code is presented in Mellema et al. (2005).

2.2 OTVET: optically thin variable Eddington tensor code (N. Gnedin, T. Abel)

The optically thin variable Eddington tensor (OTVET) approximation (Gnedin & Abel 2001) is based on the moment formulation of the RT equation

$$\begin{aligned} \frac{a}{c}\frac{\partial E_\nu}{\partial t} + \frac{\partial F_\nu^i}{\partial x^i} &= -\hat{\kappa}_\nu E_\nu + S_\nu, \\ \frac{a}{c}\frac{\partial F_\nu^j}{\partial t} + \frac{\partial}{\partial x^i} E_\nu h_\nu^{ij} &= -\hat{\kappa}_\nu F_\nu^j, \end{aligned} \tag{1}$$

where E_ν and F_ν^j are the energy density and the flux of radiation, respectively, κ_ν is the absorption coefficient, S_ν is the source function and h_ν^{ij} is a unit trace tensor normally called the Eddington tensor.

It is important to underscore that the source function $S_\nu(\boldsymbol{x})$ is considered to be an arbitrary function of position, so that it may contain both the delta-function contributions from any number of individual point sources and the smoothly varying contributions from the diffuse sources.

Equation (1) forms an open system of two partial differential equations, because the Eddington tensor cannot be determined from them. In the OTVET approximation, the Eddington tensor is computed from all sources of radiation as if they were optically thin, $h_\nu^{ij} = P_\nu^{ij}/\mathrm{Tr}\,P_\nu^{ij}$, where

$$P_\nu^{ij} = \int \mathrm{d}^3 x_1 \rho_*(\boldsymbol{x}_1) \frac{\left(x^i - x_1^i\right)\left(x^j - x_1^j\right)}{(\boldsymbol{x} - \boldsymbol{x}_1)^4},$$

where ρ_* is the mass density of the sources e.g. stars.

Thus, the OTVET approximation conserves the number density of photons (in the absence of absorption) and the flux, but may introduce an error in the direction of the flux propagation. It can be shown rigorously that the OTVET approximation is exact for a single point-like source and for uniformly distributed sources, but is not exact in other cases.

While it is difficult to prove rigorously, it appears that the largest error is introduced for the case of two sources, one much stronger than the other. In that case, the H II region around the strong source is modelled highly precisely, but the shape of the H II region around the weaker source (before the two H II regions merge) becomes ellipsoidal with the deviation from the spherical symmetry never exceeding 17 per cent (1/6) in any direction.

2.3 CRASH: cosmological RT scheme for hydrodynamics (A. Maselli, A. Ferrara, B. Ciardi)

CRASH is a 3D ray-tracing radiative-transfer code based on the Monte Carlo (MC) technique for sampling distribution functions. The grid-based algorithm follows the propagation of the ionizing radiation through an arbitrary H/He static density field and calculates the time-evolving temperature and ionization structure of the gas.

The MC approach to RT requires that the radiation field is discretized into photon packets. The radiation field is thus reproduced by emitting packets, according to the configuration under analysis, and by following their propagation accounting for the opacity of the gas. For each emitted photon packet, the emission location, frequency and propagation direction are determined by randomly sampling the appropriate probability distribution functions (PDFs), which are assigned as initial conditions. It is possible to include an arbitrary number of point/extended sources and/or diffuse background radiation in a single simulation. This approach thus allows a straightforward and self-consistent treatment of the diffuse radiation produced by H/He recombinations in the ionized gas.

The relevant radiation–matter interactions are accounted for during the photon packet's propagation. At each cell crossed, each packet deposits a fraction of its photon content according to the cell's opacity, which determines the absorption probability. Once the number of photons absorbed in the cell is calculated, we find the effect on the temperature and on the ionization state of the gas, by solving the discretized non-equilibrium chemistry and energy equations. Recombinations, collisional ionizations and cooling are treated as continuous processes.

The detailed description of the CRASH implementation is given in Ciardi et al. (2001) and Maselli, Ferrara & Ciardi (2003), and an improved algorithm for dealing with a background diffuse ionizing radiation is described in Maselli & Ferrara (2005). The tests described in this paper have been performed using the most updated version of the code (Maselli et al. 2003).

The code has been primarily developed to study a number of cosmological problems, such as hydrogen and helium reionization, the physical state of the Lyα forest, the escape fraction of Lyman continuum photons from galaxies, and the diffuse Lyα emission from recombining gas. However, its flexibility allows applications that could be relevant to a wide range of astrophysical problems. The code architecture is sufficiently simple that additional physics can be easily added using the algorithms already implemented. For example, dust absorption/re-emission can be included with minimum effort; molecular opacity and line emission, although more complicated, do not represent a particular challenge given the numerical scheme adopted. Obviously, were such processes added, the computational time could become so long that parallelization would be necessary. This would be required also when CRASH is coupled to a hydrodynamical code to study the feedback of photoprocesses on to the (thermo)dynamics of the system.

2.4 RSPH: SPH coupled with RT (H. Susa, M. Umemura)

This radiation–SPH (smoothed particle hydrodynamics) scheme is designed to investigate the formation and evolution of the first

generation objects at $z \gtrsim 10$ (Susa 2006), where the radiative feedback from various sources plays an important role. The code can compute the fractions of chemical species e, H^+, H, H^-, H_2 and H_2^+ by fully implicit time integration. It also can deal with multiple sources of ionizing radiation, as well as the radiation in the Lyman–Werner band.

Hydrodynamics is calculated by the SPH method. The code uses the version of SPH by Umemura (1993) with modifications by Steinmetz & Mueller (1993), and also adopts the particle resizing formalism by Thacker et al. (2000). In the present version, the entropy formalism is not used.

The non-equilibrium chemistry and radiative cooling for primordial gas are calculated by the code developed by Susa & Kitayama (2000), where the H_2 cooling and reaction rates are mostly taken from Galli & Palla (1998).

The on-the-spot approximation (Spitzer 1978) is used for the photoionization process. The code solves the transfer of ionizing photons directly from the source but does not solve the transfer of diffuse photons. Instead, it is assumed that the recombination photons are absorbed in the neighbourhood of the spatial position where they are emitted. The absence of a source term in this approximation greatly simplifies the radiation transfer equation. Solving the transfer equation reduces to the determination of the optical depth from the source to every SPH particle.

The optical depth is integrated utilizing the neighbour lists of SPH particles. This is similar to the code described in Susa & Umemura (2004), but is also dealing with multiple point sources. In the new scheme, the code does not create so many grid points along the light ray as the previous Susa & Umemura (2004) code did. Instead, just one grid point is created per SPH particle in its neighbourhood. The 'upstream' particle for each SPH particle is found on its LOS to the source. Then the optical depth from the source to the SPH particle is obtained by summing up the optical depth at the 'upstream' particle and the differential optical depth between the two particles.

The code is already parallelized using the Message-Passing Interface library. The computational domain is divided using the orthogonal recursive bisection method. The parallelization method for radiation transfer part is similar to the multiple wave front (MWF) method developed by Nakamoto, Umemura & Susa (2001) and Heinemann et al. (2006), but has been changed to fit the RSPH code. The details are described in Susa (2006). The code also is able to handle gravity with a Barnes–Hut tree, which is also parallelized.

2.5 ART: authentic RT with discretized long beams (T. Nakamoto, H. Susa, K. Hiroi, M. Umemura)

ART is a grid-based code designed to solve the transfer of radiation from point sources as well as diffuse radiation. On the photoionization problem, ART solves time-dependent ionization states and energies. Hydrodynamics is not incorporated into the current version.

In the first step of the ART scheme, a ray, on which photons propagate, is cast from the origin, by specifying the propagation angles. When the distance from the ray to a grid point is smaller than a certain value, a segment is located at the grid point. A collection of all the segments along the ray is considered to be a decomposition of the ray into segments. The RT calculation is sequentially done from the origin towards the downstream side on each segment. From one segment to another, the optical depth is calculated and added. Finally, changing the angle and shifting the origin, one can obtain intensities at all the grid points directed along all the angles.

ART has two versions for the integration of intensities over angle. The first is a simple summation of intensities with finite solid angles. This scheme is fit to diffuse radiation cases. The second one, designed to fit point sources, uses a solid angle of the source at the grid point to evaluate the dilution factor. Multiplying the intensity at the grid point and the dilution factor, one can obtain the integration of the intensity over angle. Generally, the radiation field can be divided into two parts: one is the direct incident radiation from point sources and the other is the diffuse radiation. ART can treat both radiation fields appropriately by using two schemes simultaneously.

The integration over frequency is done using the one-frequency method, which is similar to the six-frequency method devised by Nakamoto et al. (2001). Since in our present problems both the spectrum of the source and the frequency dependence of the absorption coefficient are known in advance, once we calculate the optical depth at the Lyman limit frequency, the amount of absorption at any frequency can be obtained without carrying out integration along the ray for the different frequency.

The parallelization of ART can be done based not only on the angle–frequency decomposition but also on the spatial domain decomposition using the MWF method (Nakamoto et al. 2001).

2.6 FTTE: fully threaded transport engine (A. Razoumov)

FTTE is a new method for the transport of both diffuse and point source radiation on refined grids developed at Oak Ridge National Laboratory. The diffuse part of the solver has been described in Razoumov & Cardall (2005). Transfer around point sources is done in a separate module acting on the same fully threaded data structure (3D fields of density, temperature, etc.) as the diffuse part. The point source algorithm is an extension of the adaptive ray-splitting scheme of Abel & Wandelt (2002) to a model with variable grid resolution, with all discretization done on the grid. Sources of radiation can be hosted by cells of any level of refinement, although usually in cosmological applications sources reside at the deepest level of refinement. Around each point source, a system of radial rays is build which split either when we move further away from the source, or when we enter a refined cell, to match the local minimum required angular resolution. Once any radial ray is refined, it stays refined (even if we leave the high spatial resolution patch) until further angular refinement is necessary.

All ray segments are stored as elements of their host cells, and actual transport just follows these interconnected data structures. Whenever possible, an attempt is made to have the most generic ray pattern possible, as each ray pattern needs to be computed only once. The simplest example is a unigrid calculation (no refinement), where there is a single-ray pattern which can be used for all sources. Another computationally trivial example is a collection of haloes within refined patches with the same local grid geometry as seen from each source.

For multiple sources located in the same H II region, we can merge their respective ray trees when the distance from the sources to a ray segment far exceeds the source separation, and the optical depth to both sources is negligible – see Razoumov et al. (2002) for details.

The transport quantity in the diffuse solver is the specific (per unit frequency) intensity, whereas in the point source solver it is the specific photon luminosity – the number of photons per unit frequency entering a particular ray segment per unit time. For discretization in angles both modules use the HEALPIX algorithm (Górski et al. 2002), dividing the entire sphere into $12 \times 4^{n-1}$ equal area pixels, where $n = 1, 2, \ldots$ is the local angular resolution. For point source transfer, n is a function of the local grid resolution, the physical distance to

the source and the local ray pattern in a cell. As we go from one ray segment to another, in each cell the code accumulates the mean diffuse intensity and all photoreaction rates due to point source radiation. For rate equations, the time-dependent chemistry solver from Anninos et al. (1997) is used.

Currently, there is only a serial version of the code, although there is a project underway at the San Diego Supercomputing Center to parallelize the diffuse part of the algorithm angle-by-angle. Even in the serial mode the code is very fast, limited in practice by the memory available to hold ray patterns. Various test problems up to grid sizes 256^3 with five levels of refinement (8192^3 effective spatial resolution), and up to the angular resolution level $n = 13$ have been run.

2.7 SIMPLEX: RT on unstructured grids (J. Ritzerveld, V. Icke, E.-J. Rijkhorst)

SIMPLEX (Ritzerveld, Icke & Rijkhorst 2003) is a mesoscopic particle method, using unstructured Lagrangian grids to solve the Boltzmann equation for a photon gas. It has many similarities with lattice Boltzmann solvers, which are used in complex fluid flow simulations, with the exception that it uses an adaptive grid based on the criterion that the local grid step is chosen to correlate with the mean free path of the photon. In the optimal case, this last modification results in an operation count for our method which does *not* scale with the number of sources.

More specifically, SIMPLEX does not use a grid in the usual sense, but has as a basis a point distribution, which follows the density, or opacity of the medium. Given a regular grid with medium density values, a MC method is used to sample our points according to this density distribution. An unstructured grid is constructed from this point distribution by using the Delaunay tessellation technique. This recipe was intentionally chosen this way to ensure that the local optical mean free paths correlate linearly with the line lengths between points. This way, the radiation–matter interactions, which determine the collision term on the right-hand side of the Boltzmann equation, can be incorporated by introducing a set of 'interaction coefficients' $\{c_i\}$, one for each interaction. These coefficients are exactly the linear correlation coefficients between the optical mean free path and the local line lengths.

The transport of radiation through a medium can subsequently be defined and implemented as a walk on this resultant graph, with the interaction taking place at each node. The operation count of this resultant method is $O(N^{1+1/m})$, in which N is the number of points, or resolution and m is the dimension. This is *in*dependent of the number of sources, which makes it ideal to do large-scale reionization calculations, in which a large number of sources is needed.

The generality of the method's set-up defines its versatility. Boltzmann-like transport equations describe not only the flow of a photon gas, but also that of a fluid or that of a plasma. It is therefore straightforward to define a SIMPLEX method which solves both the RT equations and the hydrodynamics equations self-consistently. The process of making a dynamic coupling of SIMPLEX with the grid-based hydrocodes FLASH (Fryxell et al. 2000) and GADGET-2 (Springel 2005) is under way. The code easily runs on a single desktop machine, but will be parallelized in order to accommodate this coupling.

For this comparison project, the SIMPLEX method was set up to do cosmological RT calculations. The result is a method which is designed to be photon conserving, updating the ionization fraction and the resultant exact local optical depth dynamically throughout the simulation. Moreover, diffuse recombination radiation, shown to be quite important for the overall result (e.g. Ritzerveld 2005), can readily be implemented self-consistently and without loss of computational speed. The code can run with either periodic or transmissive boundary conditions.

For now, we do not solve the energy equation, and do simulations of H-only. We ignore the effect of spectral hardening, as a result of which we can analytically derive the fraction of the flux above the Lyman limit, given that the source radiates as a blackbody. We account for H-absorption by using a blackbody-averaged absorption coefficient. The final results are interpolated from the unstructured grid cells on to the 128^3 data cube to accommodate this comparison.

2.8 ZEUS-MP with RT (D. Whalen, M. Norman)

The ZEUS-MP hydrocode in this comparison project solves explicit finite-difference approximations to Euler's equations of fluid dynamics together with a nine-species reactive network that utilizes photoionization rate coefficients computed by a ray-casting RT module (Whalen & Norman 2006). Ionization fronts thus arise as an emergent feature of reactive flow and RT in our simulations and are not tracked by computing equilibria positions along LOSs. The hydrodynamical variables (ρ, e, and the ρv_i) are updated term by term in operator-split and directionally split substeps, with a given substep incorporating the partial update from the previous substep. The gradient (force) terms in the Euler equations are computed in source routines and the divergence terms are calculated in advection routines (Stone & Norman 1992).

The primordial species added to ZEUS-MP (H, H^+, He, He^+, He^{2+}, H^-, H_2^+, H_2 and e^-) are evolved by nine additional continuity equations and the non-equilibrium rate equations of Anninos et al. (1997). The divergence term for each species is evaluated in the advection routines, while the other terms form a reaction network that is solved separately from the source and advective updates. Although the calculations performed for this comparison study take the gas to be hydrogen only, in general we sequentially advance each n_i in the network, building the ith species' update from the $i - 1$ (and earlier) updated species, while applying rate coefficients evaluated at the current problem time. Charge and baryon conservation are enforced at the end of each hydrodynamic cycle and microphysical cooling and heating processes are included by an isochoric operator-split update to the energy density computed each time the reaction network is advanced. The RT module computes the photoionization rate coefficients required by the reaction network by solving the static equation of transfer, recast into flux form along radial rays outwards from a point source centred in a spherical-coordinate geometry. The number of ionizations in a zone is calculated in a photon-conserving manner to be the number of photons entering the zone minus the number exiting.

The order of execution of the algorithm is as follows. First, the RT module is called to calculate ionization rates in order to determine the smallest heating/cooling time on the grid. The grid minimum of the Courant time is then computed and the hydrodynamics equations are evolved over the smaller of the two time-scales. Next, the shortest chemistry time-scale of the grid is calculated

$$\Delta t_{\rm chem} = 0.1 \frac{n_{\rm e}}{\dot{n}_{\rm e}} \tag{2}$$

which is formulated to ensure that the fastest reaction operating at any place or time in the problem governs the maximum time by which the reaction network may be accurately advanced. The species concentrations and gas energy are then advanced over this time-step,

the transfer module is called again to compute a new chemistry time-step, and the network and energy updates are performed again. The n_i and energy are subcycled over successive chemistry time-steps until the hydrodynamical time-step has been covered, at which point full updates of velocities, energies and densities by the source and advection routines are computed. A new hydrodynamical time-step is then determined and the cycle repeats.

This algorithm has been extensively tested with a comprehensive suite of quantitative static and hydrodynamical benchmarks complementing those appearing in this paper. The tests are described in detail in Whalen & Norman (2006).

2.9 FLASH-HC: hybrid characteristics (E.-J. Rijkhorst, T. Plewa, A. Dubey, G. Mellema)

The hybrid characteristics (HC) method (Rijkhorst 2005; Rijkhorst et al. 2006) is a three-dimensional RT algorithm designed specifically for use with parallel adaptive mesh refinement (AMR) hydrodynamics codes. It introduces a novel form of ray tracing that can be classified as neither long nor short characteristics. It, however, does apply the underlying principles, i.e. efficient execution through interpolation and parallelizability, of both these approaches.

Primary applications of the HC method are radiation hydrodynamics problems that take into account the effects of photoionization and heating due to point sources of radiation. The method is implemented into the hydrodynamics package FLASH (Fryxell et al. 2000). The ionization, heating and cooling processes are modelled using the DORIC package (Frank & Mellema 1994). Upon comparison with the long characteristics method, it was found that the HC method calculates shadows with similarly high accuracy. Although the method is developed for problems involving photoionization due to point sources, the algorithm can easily be adapted to the case of more general radiation fields.

The HC algorithm can be summarized as follows. Consider an AMR hierarchy of grids that is distributed over a number of processors. Rays are traced over these different grids and must, to make this a parallel algorithm, be split up into independent ray sections. Naturally, these sections are in the first place defined by the boundaries of each processor's subdomain, and in the second place by the boundaries of the grids contained within that subdomain. At the start of a time-step, each processor checks if its subdomain contains the source. The processor that owns the source stores its grid and processor identification and makes it available to all other processors. Then each processor ray traces the grids it owns to obtain local column density contributions. Since in general rays traverse more than one processor domain, these local contributions are made available on all processors through a global communication operation. By interpolating and accumulating all contributions for all rays (using a so-called grid mapping), the total column density for each cell is obtained. The coefficients used in the interpolation are chosen such that the exact solution for the column density is retrieved when there are no gradients in the density distribution. Tests with a $1/r^2$ density distribution resulted in errors <0.5 per cent in the value for the total column density as compared to a long characteristics method.

Once the column density from the source up to each cell face is known, the ionization fractions and temperature can be computed. For this, we use the DORIC package (see Frank & Mellema 1994; Mellema & Lundqvist 2002). These routines calculate the photo- and collisional ionization, the photoheating and the radiative cooling rate. Using an analytical solution to the rate equation for the ionization fractions, the temperature and ionization fractions are found through an iterative process. Since evaluating the integrals for the photoionization and heating rate is too time consuming to perform for every value of the optical depth, they are stored in look-up tables and are interpolated when needed.

The hydrodynamics and ionization calculations are coupled through operator splitting. To avoid having to take time-steps that are the minimum of the hydrodynamics, ionization and heating/cooling time-scales, the code uses the fact that the equations for the ionization and heating/cooling can be iterated to convergence. This means that the only restriction on the time-step comes from the hydrodynamics (i.e. the Courant condition). Note, however, that when one needs to follow R-type (i.e. which are much faster than the gas response to it) ionization fronts, an additional time-step constraint is used to find the correct propagation velocity for this type of front.

An assessment of the parallel performance of the HC method was presented by Rijkhorst (2005). It was found that the ray-tracing part takes less time to execute than other parts of the calculation (e.g. hydrodynamics and AMR.). Tests involving randomly distributed sources show that the algorithm scales linearly with the number of sources. Weak scaling tests, where the amount of work per processor is kept constant, as well as strong scaling tests, where the total amount of work is kept constant, were performed as well. By carefully choosing the amount of work per processor, it was shown that the HC algorithm scales well for at least $\sim$100 processors on a SGI Altix, and $\sim$1000 processors on an IBM BlueGene/L system.

The HC method will be made publicly available in a future FLASH release.

2.10 IFT: ionization front tracking (M. Alvarez and P. Shapiro)

IFT is a ray-tracing code which explicitly follows the progress of an ionization front (I-front) around a point source of ionizing radiation in an arbitrary three-dimensional density field of atomic hydrogen. Because it does not solve the non-equilibrium chemical and energy rate equations and uses a simplified treatment of RT, our method is extremely fast. While the code is currently capable of handling only one source, it is being generalized to handle an arbitrary number of point sources. More detailed descriptions of various aspects of this code can be found in section 5.1.3 of Mellema et al. (2006a) and section 3 of Alvarez, Bromm & Shapiro (2006).

The fundamental assumption is that the I-front is sharp. Behind the front, the ionized fraction and temperature are assumed to take their equilibrium values, while ahead of the front they are assigned their initial values. The assumption of equilibrium behind the I-front is justified because the equilibration time on the ionized side of the I-front is shorter than the recombination time by a factor of the neutral fraction, which is small behind the I-front. Because the progress of the I-front will be different in different directions, it is necessary to solve for its time-dependent position along rays that emanate from the source, the angular orientation of which is chosen to lie at the centres of HEALPIXELS[1] (Górski et al. 2005). Typically, we choose a sufficient resolution of rays in the sky such that there is approximately one ray per edge cell. Along a given ray, we solve the fully relativistic equation for the propagation of the I-front (Shapiro et al. 2005):

$$\frac{\mathrm{d}R}{\mathrm{d}t} = \frac{cQ(R)}{Q(R) + 4\pi R^2 cn(R)}, \tag{3}$$

where $Q(R)$ is the ionizing photon luminosity at the surface of the

[1] http://healpix.jpl.nasa.gov

front, R is the distance along the ray and c is the speed of light. This equation correctly accounts for the finite traveltime of ionizing photons, i.e. as $Q(R) \longrightarrow \infty$, $\mathrm{d}R/\mathrm{d}t \longrightarrow c$. The arrival rate of ionizing photons is given by

$$Q(R) = Q_* - 4\pi \int_0^R \alpha_{\mathrm{B}}(r) n^2(r) r^2 \, \mathrm{d}r, \quad (4)$$

where Q_* is the ionizing photon luminosity of the source, $n(r)$ is the density along the ray, and $\alpha_{\mathrm{B}}(r)$ is the 'Case B' recombination coefficient along the ray. The value of $\alpha_{\mathrm{B}}(r)$ is determined by the equilibrium temperature, which varies along the ray.

A brief outline of the algorithm is as follows. First, the code interpolates the density from the grid to discrete points along each ray, where the spacing between points along each ray is approximately the same as the cell size of the grid. Next, it computes the equilibrium profile of ionized fraction and temperature along each ray by moving outwards from the source, using the equilibrium neutral hydrogen density of the previous zones to attenuate the flux to each successive zone. Equation (3) is then solved for each ray, which gives the I-front position in that direction. The values of ionized fraction and temperature along each ray are set to their equilibrium values inside of the I-front, and set to their initial values on the outside. Finally, the ionized fraction and temperature are interpolated back from the rays to the grid.

2.11 CORAL (I. Iliev, A. Raga, G. Mellema, P. Shapiro)

CORAL is a 2D, axisymmetric Eulerian fluid dynamics AMR code (see Mellema et al. 1998; Shapiro, Iliev & Raga 2004, and references therein for detailed description). It solves the Euler equations in their conservative finite-volume form using the second-order method of van Leer flux splitting, which allows for correct and precise treatment of shocks. The grid refinement and derefinement criteria are based on the gradients of all code variables. When the gradient of any variable is larger than a pre-defined value the cell is refined, while when the criterion for refinement is not met the cell is derefined.

The code follows, by a semi-implicit method, the non-equilibrium chemistry of multiple species (H, He, C II–VI, N I–VI, O I–VI, Ne I–VI and S II–VI) and the corresponding cooling (Raga, Mellema & Lundqvist 1997; Mellema et al. 1998), as well as Compton cooling. The photoheating rate used is a sum of the photoionization heating rates for H I, He I and He II. For computational efficiency, all heating and cooling rates are pre-computed and stored in tables. The microphysical processes – chemical reactions, radiative processes, transfer of radiation, heating and cooling – are implemented though the standard approach of operator splitting (i.e. solved at each time-step, side-by-side with the hydrodynamics and coupled to it through the energy equation). The latest versions of the code also include the effects of an external gravity force.

Currently, the code uses a blackbody, or a power-law ionizing source spectrum, although any other spectrum can be accommodated. RT of the ionizing photons is treated explicitly by taking into account the bound-free opacity of H and He in the photoionization and photoheating rates. The photoionization and photoheating rates of H I, He I and He II are pre-computed for the given spectrum and stored in tables versus the optical depths at the ionizing thresholds of these species, which are then used to obtain the total optical depths. The code correctly tracks both fast (by evolving on an ionization time-step, $\Delta t \sim \dot{n_{\mathrm{H}}}/n_{\mathrm{H}}$) and slow I-fronts.

The code has been tested extensively and has been applied to many astrophysical problems, e.g. photoevaporation of clumps in planetary nebulae (Mellema et al. 1998), cosmological minihalo photoevaporation during reionization (Shapiro, Iliev & Raga 2004; Iliev, Shapiro & Raga 2005) and studies of the radiative feedback from propagating ionization fronts on dense clumps in damped Lyman α systems (Iliev, Hirashita & Ferrara 2006a).

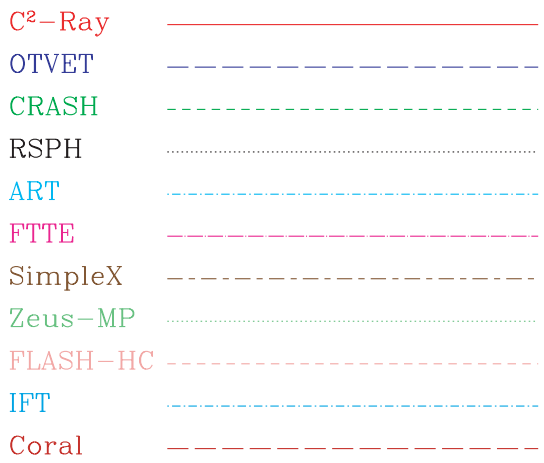

Figure 1. Legend for the line plots.

3 TESTS AND RESULTS

In this section, we describe the tests we have performed, along with their detailed parameters, geometry and set-up and the results we obtained. When constructing these tests, we aimed for the simplest and cleanest, but none the less chose cosmologically interesting problems. We designed them in a way which allows us to test and compare all the important aspects of any radiative-transfer code. These include correct tracking of both slow and fast I-fronts, in homogeneous and inhomogeneous density fields, formation of shadows, spectrum hardening and solving for the gas temperature state. In a companion paper (Paper II), we will present tests which include the interaction with fluid flows and radiative feedback on the gas. For simplicity, in all tests the gas is assumed to be hydrogen only. The gas density distribution is fixed. Finally, in order to be included in the comparison, each test had to be carried out by at least three or more of the participating codes.

Fig. 1 provides a legend allowing the reader to identify which line type and colour correspond to which code in the line plots throughout the paper. The images are labelled with the code name and also identified in the corresponding figure caption.

All test problems are solved in three dimensions (3D), with grid dimensions 128^3 cells. For the 1D (ZEUS-MP) and 2D (CORAL) codes the data are interpolated on the same size 3D grid and analysed the same way. Unless otherwise noted, the sources of ionizing radiation are assumed to have a blackbody spectrum with effective temperature $T_{\mathrm{eff}} = 100\,000$ K, except for Test 1 where the assumed spectrum is monochromatic with all photons having energy $h\nu = 13.6$ eV, the ionization threshold of hydrogen. In all tests, the temperature is allowed to vary due to atomic heating and cooling processes in accordance with the energy equation, again with the exception of Test 1 where we fix the temperature at $T = 10^4$ K. The few codes that do not yet include an energy equation use a constant temperature value.

3.1 Test 0. The basic physics

The solution of the RT equation is intimately related to the ionization and thermal states of the gas. These depend on the atomic physics

Table 2. Rates adopted by the different RT codes. The columns are, from left to right, name of the code and reference for: Case A recombination rate, α_A (RRA), of H II, He II and He III; Case B recombination rate, α_B (RRB), of H II, He II and He III; dielectronic recombination rate (DRR) of He II; collisional ionization rate (CIR), of H I, C_{HI}, He I, C_{HeI} and He III, C_{HeII}; collisional ionization cooling rate, Λ ion (CICR) of H I, He I and He II; Case A recombination cooling rate, Λ rec, A (RCRA), of H II, He II and He III; Case B recombination cooling rate, Λ rec, B (RCRB), of H II, He II and He III; dielectronic recombination cooling rate (DRCR) of He II; collisional excitation cooling rate, Λ line (CECR), of H I, He I and He II; bremsstrahlung cooling rate, Λ ff (BCR); Compton cooling rate (CCR); cross-section, σ (CS), of H I, He I and He II. Units of RRA, RRB, DRR and CIR are (cm^3 s^{-1}), units of CICR, RCRA, RCRB, DRCR, CECR, BCR, CCR are (erg cm^3 s^{-1}) and units of CS are (cm^2). Note that for those codes in which the treatment of He is not included, only the references to the H rates are given.

Code	RRA	RRB	DRR	CIR	CICR	RCRA	RCRB	DRCR	CECR	BCR	CCR	CS
C^2-RAY		10, 11, 10		6			10, 11, 10		23, –, –	10	18	15
OTVET	9, 4, 9	9, 4, 9	2	9, 9, 9	9, 9, 9	9, 4, 9	9, 4, 9	2	5, –, 5		17	22
CRASH	5, 5, 5	20, 20, 20	5	5, 5, 5	5, 5, 5	5, 5, 5	20, 20, 20	5	5, 5, 5	5	8	15
RSPH		20		18			20		7			18
ART	19	20		19		19	20		19	19	19	13
FTTE	1	9, 9, 9	1	1, 1, 1	18, 18, 18	5, 5, 5	10, 11, 10	5	3, 5, 5	3	16	15
SIMPLEX		20		6								15
ZEUS-MP	1	21		12	18	5			5, –, –	3	16	14
FLASH-HC		10, 11, 10		6			10, 11, 10		23, –, –	10		15
IFT		9		25	5		18		5, –, –	3		22
CORAL	10, 11, 10	10, 11, 10	24	6	23, 23, 23	10, 11, 10	10, 11, 10	24	23, 23, 23	10	18	15

(1) Abel et al. (1997); (2) Aldrovandi & Pequignot (1973); (3) Black (1981); (4) Burgess & Seaton (1960); (5) Cen (1992); (6) Cox (1970); (7) Fukugita & Kawasaki (1994); (8) Haiman, Thoul & Loeb (1996); (9) Hui & Gnedin (1997); (10) Hummer (1994); (11) Hummer & Storey (1998); (12) Janev, Langer & Evans (1987); (13) Lang (1974); (14) Osterbrock (1974); (15) Osterbrock (1989); (16) Peebles (1971); (17) Peebles (1993); (18) Shapiro & Kang (1987); (19) Sherman (1979); (20) Spitzer (1978); (21) Tenorio-Tagle et al. (1986); (22) Verner et al. (1996); (23) Aggarwal (1983); (24) Raga et al. (1997); (25) Voronov (1997).

Notes. The codes C^2-RAY, FLASH-HC and CORAL all share the same non-equilibrium chemistry module (DORIC, developed by G. Mellema), so they have the same hydrogen chemistry and heating rates and cross-section, and the same chemistry solver. However, CORAL also includes the chemistry of helium and a number of metals. We also note that for the CECR rate, references (3), (5) and (7) are based on Dalgarno & McCray (1972), while reference (19) is based on Tucker & Gould (1966).

reaction rates, photoionization cross-sections, as well as the cooling and heating rates used. As there are a variety of rates available in the literature, for the sake of clarity we have summarized those used in our codes in Table 2 and plotted the main hydrogen rates in Fig. 2. The table columns indicate, from left to right, the name of the code and the reference for: Case A recombination rate of H II, He II and He III; Case B recombination rate of H II, He II and He III; dielectronic recombination rate of He II; collisional ionization rate of H I, He I and He III; collisional ionization cooling rate of H I, He I and He II; Case A recombination cooling rate of H II, He II and He III; Case B recombination cooling rate of H II, He II and He III; dielectronic recombination cooling rate of He II; collisional excitation cooling rate of H I, He I and He II; bremsstrahlung cooling rate; Compton cooling rate; cross-section of H I, He I and He II. Note that for those codes in which the treatment of He is not included, only the references to the H rates are given.

The first thing to note in Fig. 2 is that although the rates come from a wide variety of sources, they largely agree. We also note that some of the rates are very similar, even identical, even if they at first sight seem to be originating from different sources in the literature. This is due to the fact that for some rates only a few primary sources exist. These rates are then used in later works and not always referred to the original source (see the note below Table 2). The main differences are in our recombination cooling rates, particularly at very high temperatures, beyond the typical range of gas temperatures achieved by photoionization heating ($T \lesssim 10^5$ K). It should be noted, however, that e.g. shock-heated gas can reach much higher temperatures, in which case the differences in our rates become very large and caution should be exercised in choosing the appropriate rates. However, even at the typical photoionization temperatures there are differences between the rates by up to factors of $\sim$2. The origin of these discrepancies is currently unclear, and it is also unclear which fit to the experimental data is more precise. There are also a few cases in which particular cooling rates (e.g. ZEUS Case B recombination cooling, ART line cooling) are notably different from the rest.

As a next step, we performed several numerical experiments to assess the offsets between our results that can arise solely based on our different chemistry and cooling rates. We did this by implementing the rates from several codes representative of the full range of rates present above into a single code (1D version of the ART code) and running the same problem (Test 2 described below, which is the expansion of a H II region in uniform density gas, see Section 3.3 for detailed test definition and solution features). In all cases, the same photoionization cross-section (the one of ART) is used and only the rates are varied. The code OTVET here stands also for the codes C^2-RAY, CRASH, FLASH-HC and CORAL, since all these codes have either identical, or closely matching rates. Results are shown in Figs 3 and 4. In Fig. 3, we show the I-front position, r_I, and the I-front velocity, v_I (both quantities are normalized to the analytical solutions of that problem obtained at temperature $T = 10^4$ K, while the time is in units of the recombination time at the same temperature). Note that the results for ZEUS use the recombination cooling rate of ART since its currently implemented rate is oversimplified. We show the results using the rates of OTVET, FTTE, RSPH, ZEUS-MP and ART.

Initially, when the I-front is fast and still far away from reaching its Strömgren sphere the results for all codes agree fairly well, as expected since recombinations are still unimportant. Once recombinations do become important, at $t > t_{rec}$, the results start diverging. The results for OTVET, FTTE and RSPH remain in close agreement, within a fraction of a per cent in the I-front radius and within $\sim$2 per

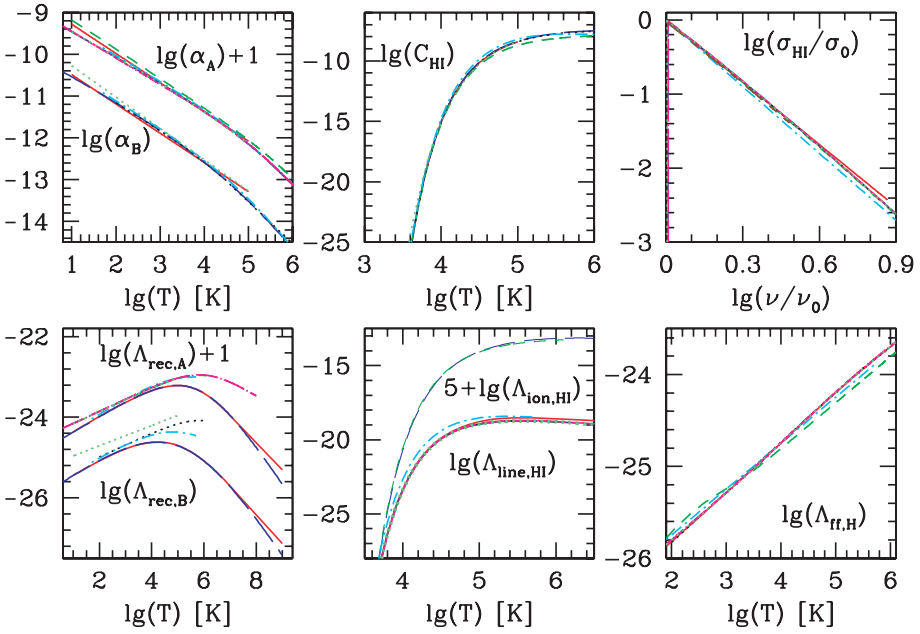

Figure 2. Test 0, Part 1. Hydrogen rates, cooling and cross-sections used by the participating codes: Case A recombination rate, $\alpha_{\rm A}$; Case B recombination rate, $\alpha_{\rm B}$; collisional ionization rate, $C_{\rm HI}$; cross-section, $\sigma_{\rm HI}/\sigma_0$, normalized to the value at the ionization threshold; collisional ionization cooling rate, $\Lambda_{\rm ion,HI}$; Case A recombination cooling rate, $\Lambda_{\rm rec,A}$; Case B recombination cooling rate, $\Lambda_{\rm rec,B}$; collisional excitation cooling rate, $\Lambda_{\rm line,HI}$; bremsstrahlung cooling rate for hydrogen, $\Lambda_{\rm ff,H}$. Units of $\alpha_{\rm A}, \alpha_{\rm B}$ and $C_{\rm HI}$ are (cm^3 s^{-1}), units of the cooling rates are (erg cm^3 s^{-1}) and units of cross-sections are (cm^2).

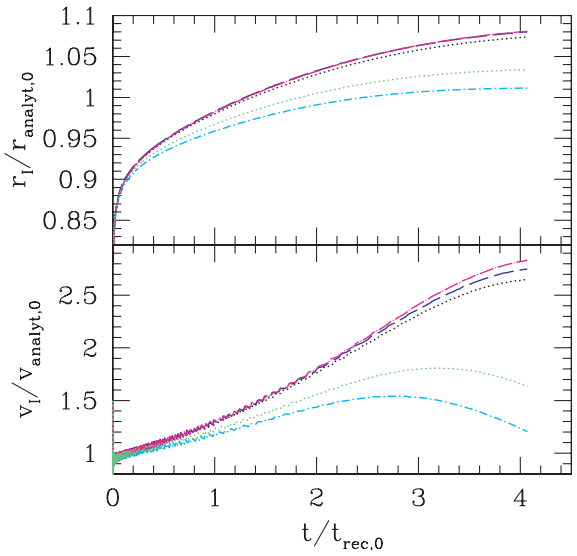

Figure 3. Test 0, Part 2. I-front expansion in uniform density field with temperature evolution (same as Test 2 below). Plotted are the I-front position (top panel) and velocity (bottom panel) all derived from the same code (1D, spherically symmetric version of the ART code) and using the photoionization cross-section from that code, but with the rest of the microphysics (chemistry and cooling rates) taken from several of the participating codes, as indicated by line-type and colour. All results are normalized to the analytical ones (which assume fixed temperature, $T = 10^4$ K) given in equation (5) below (see the text for details).

cent in the I-front velocity. The results using the ZEUS and ART rates, however, depart notably from the others, by up to 4 and 6 per cent, respectively, in radius. The corresponding velocities are different by even more, up to a factor of ∼2 at the end, when the I-front is close to stationary. In Fig. 4, we show the radial profiles of the ionized fraction x, and temperature T, normalized to the results using OTVET rates (left-hand panel), and in absolute units (right-hand panel). The ionized fraction profiles for ART and ZEUS again are fairly different from the rest, by 20–40 per cent, while the rest of the codes agree between themselves much better, to less than 10 per cent. Agreement is slightly worse close to the ionizing source. In terms of temperature profiles, the codes agree to better than 10 per cent, with the exception of ART, in which case the resulting temperature is notably lower, by ∼20 per cent.

The reasons for these discrepancies lie largely in differences in the recombination rates and the recombination and line cooling rates. Since the collisional excitation cooling rates of hydrogen are categorized into those by two original papers as shown in the notes of Table 2, the results are separated into two groups in the same way. The line cooling rate of ART is larger than the ones for most of the other codes by a factor of 2–5 in the temperature range 10^4–10^5 K, while the recombination rate used by that code is about 10–15 per cent larger in the same temperature range, thus the resulting gas temperature is correspondingly lower. This lower temperature results in a higher recombination rate and hence the slower propagation of the I-front we observed. The reason for the discrepancy with ZEUS is mostly due to its higher recombination rate. This again results in a somewhat slower I-front propagation, but not in significant temperature differences. Accordingly, for both of these codes the neutral gas fraction is significantly higher at all radii. The slightly higher recombination cooling of RSPH results in slightly lower temperature and proportionally higher neutral fraction, although both are off by only a few per cent, and up to 10 per cent close to the ionizing source.

The last important element in this basic physics comparison is to assess the accuracy and robustness of the methods we use for solving the non-equilibrium chemistry equations. These equations are stiff and thus generally require implicit solution methods. Such methods

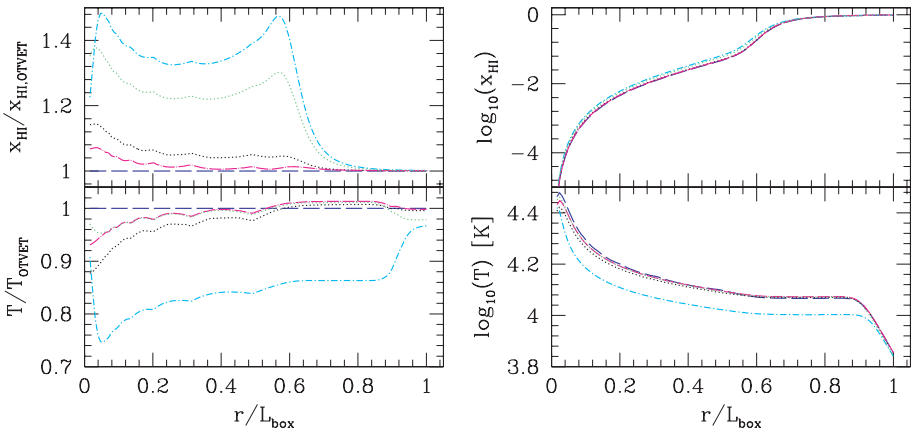

Figure 4. Test 0, Part 2. The same test as in Fig. 3. Left-hand panel: (a) the radial profiles of the neutral fraction (top, normalized to the result which uses the OTVET rates), temperature (middle, again normalized to the results for OTVET rates) at time $t = 100$ Myr=$0.82t_{rec,0}$. Right-hand panel: (b) the same as in (a) but in absolute units.

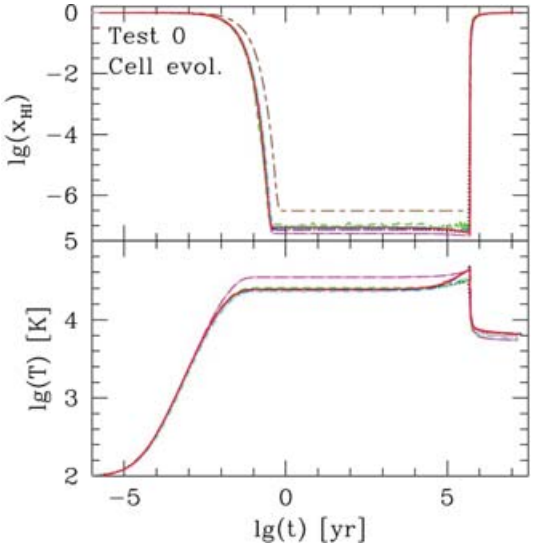

Figure 5. Test 0, Part 3. Single-zone ionizing, cooling and recombining.

are generally expensive, however, so often certain approximations are used to speed up the calculations. In order to test them, we performed the following simple test with a single, optically thin zone. We start with a completely neutral zone at time $t = 0$. We then apply a photoionizing flux of $F = 10^{12}$ photons s^{-1} cm^{-2}, with a 10^5 K blackbody spectrum for 0.5 Myr, which results in the gas parcel becoming heated and highly ionized. Thereafter, the ionizing flux is switched off and the zone cools down and recombines for a further 5 Myr. The zone contains only hydrogen gas with number density of $n = 1$ cm^{-3} and initial temperature of $T_i = 100$ K. These results are shown in Fig. 5.

All codes agree very well in terms of the evolution of the neutral fraction (top panel), with the sole exception of SIMPLEX, in which case both the speed with which the gas parcel ionizes and the achieved level of ionization are significantly different from the rest. The reason for this discrepancy is that currently this code does not solve the energy equation to find the gas temperature, but has to assume a value instead ($T = 10^4$ K in this test). FTTE finds slightly higher temperatures after its initial rise and correspondingly lower neutral fractions.

Some differences are also seen after time $t \sim 0.1$ Myr, at which point there is a slight rise in temperature and corresponding dip in the neutral fraction. These occur around the time when the recombinations start becoming important, $t_{rec} \sim 0.1$ Myr, which gives rise to slight additional heating. About half of the codes predict somewhat lower temperature rises than the rest. The cooling/recombination phase after source turn-off demonstrates good agreement between the codes, although there are small differences in the final temperatures reached. This is due to small differences in the hydrogen-line cooling rates, resulting in slightly different temperatures at which the cooling becomes inefficient.

3.2 Test 1. Pure hydrogen isothermal H II region expansion

This test is the classical problem of a H II region expansion in uniform gas around a single ionizing source (Strömgren 1939; Spitzer 1978). A steady, monochromatic ($h\nu = 13.6$ eV) source emitting $\dot{N}_\gamma$ ionizing photons per unit time is turning on in an initially neutral, uniform density, static environment with hydrogen number density n_H. For this test, we assume that the temperature is fixed at $T = 10^4$ K. Under these conditions, and if we assume that the front is sharp (i.e. that it is infinitely thin, with the gas inside fully ionized and the gas outside fully neutral) there is a well-known analytical solution for the evolution of the I-front radius, r_I, and velocity, v_I, given by

$$r_I = r_S \left[1 - \exp(-t/t_{rec})\right]^{1/3},$$
$$v_I = \frac{r_S}{3t_{rec}} \frac{\exp(-t/t_{rec})}{[1 - \exp(-t/t_{rec})]^{2/3}}, \quad (5)$$

where

$$r_S = \left[\frac{3\dot{N}_\gamma}{4\pi\alpha_B(T)n_H^2}\right]^{1/3} \quad (6)$$

is the Strömgren radius, i.e. the final, maximum size of the ionized region at which point recombinations inside balance the incoming photons and the H II region expansion stops. The Strömgren radius is obtained from

$$F = \int_0^{rs} d\ell n_e n_H \alpha_B(T), \quad (7)$$

i.e. by balancing the number of recombinations with the number of ionizing photons arriving along a given LOS. Here, n_e is the electron

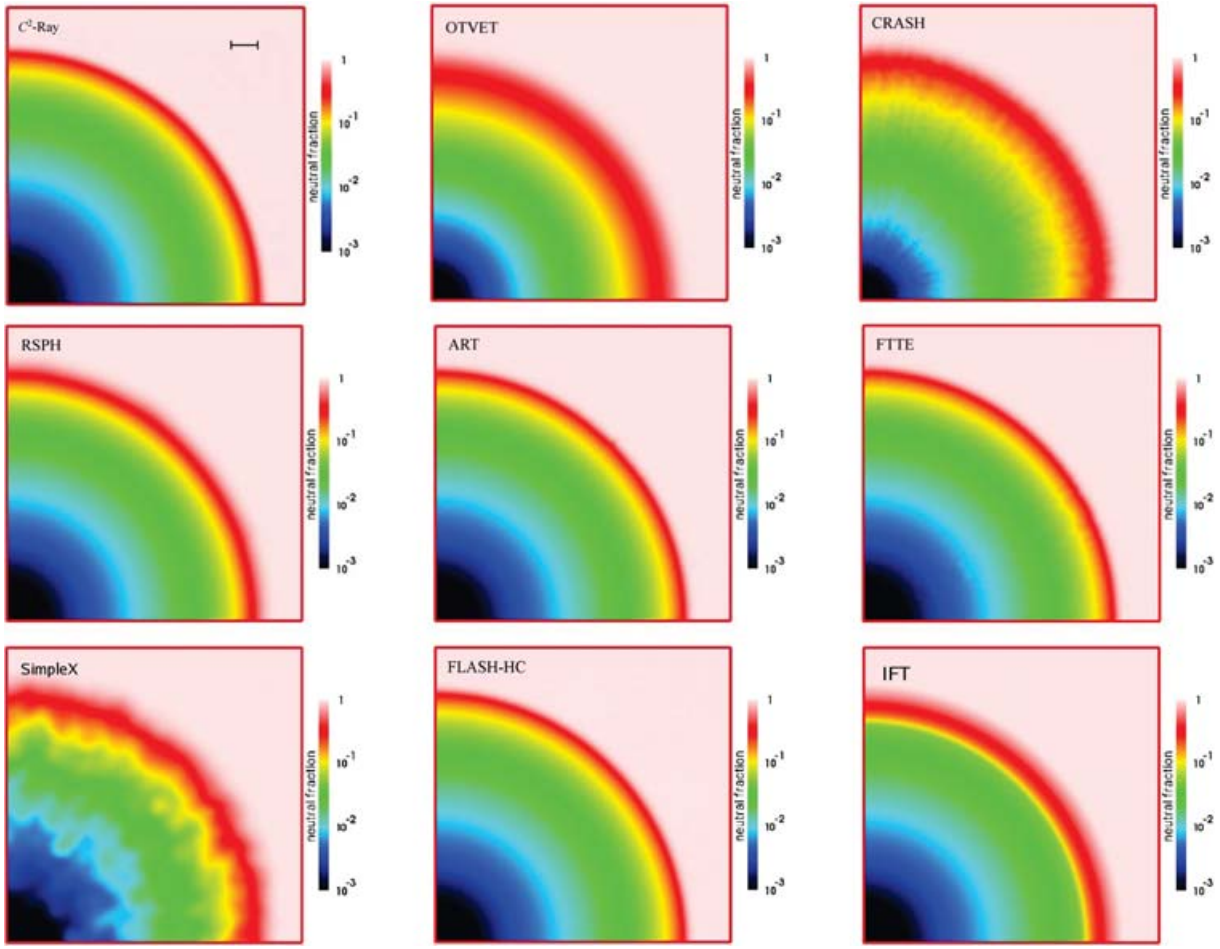

Figure 6. Test 1 (H II region expansion in a uniform gas at fixed temperature): images of the H I fraction, cut through the simulation volume at coordinate $z = 0$ at time $t = 500$ Myr (final Strömgren sphere) for (left to right and top to bottom) C^2-RAY, OTVET, CRASH, RSPH, ART, FTTE, SIMPLEX, FLASH-HC and IFT.

density,

$$t_{\rm rec} = [\alpha_{\rm B}(T) n_{\rm H}]^{-1}, \tag{8}$$

is the recombination time, and $\alpha_{\rm B}(T)$ is the Case B recombination coefficient of hydrogen in the ionized region at temperature T. The H II region initially expands quickly and then slows considerably as the evolution time approaches the recombination time, $t \sim t_{\rm rec}$, at which point the recombinations start balancing the ionizations and the H II region approaches its Strömgren radius. After a few recombination times the I-front stops at radius $r_{\rm I} = r_{\rm S}$, and in the absence of gas motions remains static thereafter. The photon mean free path is given by

$$\lambda_{\rm mfp} = \frac{1}{n_{\rm H}\sigma_0} = 0.041\,{\rm pc}. \tag{9}$$

The particular numerical parameters we used for this test are as follows. Computational box dimension $L = 6.6$ kpc; gas number density $n_{\rm H} = 10^{-3}$ cm^{-3}; initial ionization fraction (given by collisional equilibrium) $x = 1.2 \times 10^{-3}$; and ionization rate $\dot{N}_\gamma = 5 \times 10^{48}$ photons s^{-1}. The source is at the corner of the box). For these parameters, the recombination time is $t_{\rm rec} = 3.86 \times 10^{15}$ s $= 122.4$ Myr. Assuming a recombination rate $\alpha_{\rm B}(T) = 2.59 \times 10^{-13}$ cm^3 s^{-1} at $T = 10^4$ K, then $r_{\rm S} = 5.4$ kpc. The simulation time is $t_{\rm sim} = 500$ Myr $\approx 4\,t_{\rm rec}$. The required outputs are the neutral fraction of hydrogen on the whole grid at times $t = 10, 30, 100, 200$ and 500 Myr, and the I-front position (defined by the 50 per cent neutral fraction) and velocity versus time along the x-axis.

In Fig. 6, we show images of the neutral fraction in the $z = 0$ plane at time $t = 500$ Myr, at which point the equilibrium Strömgren sphere is reached. The size of the final-ionized region is in very good agreement between the codes. In most cases, the H II region is nicely spherical, although some anisotropies exist in the CRASH and SIMPLEX results. In the first case, these are due to the MC random sampling nature of this code, while in the second case it is due to the unstructured grid used by that code, which had to be interpolated on the regular grid format used for this comparison. There are also certain differences in the H II region ionized structure, e.g. in the thickness of the ionized-neutral transition at the Strömgren sphere boundary. The inherent thickness of this transition (defined as the radial distance between 0.1 and 0.9 ionized fraction points) for a monochromatic spectrum is $\approx 18\lambda_{\rm mfp} = 0.74$ kpc, or about 14 simulation cells, equal to 11 per cent of the simulation box size. This thickness is indicated in the upper left-hand panel of Fig. 6. Most codes yield widths which are very close to this expected value. Only the OTVET, CRASH and SIMPLEX codes find thicker transitions due to the inherently greater diffusivity of these methods, which spreads out the transition. For the same reason, the highly ionized proximity region of the source (blue–black colours) is notably smaller for the first two of these codes.

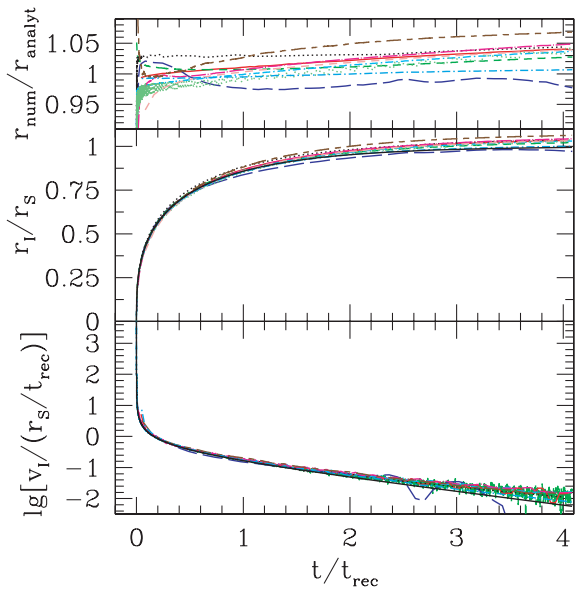

Figure 7. Test 1 (H II region expansion in a uniform gas at fixed temperature): the evolution of the position and velocity of the I-front.

In Fig. 7, we show the evolution of the I-front position and velocity. The analytical results in equation (5) are shown as well (black, solid lines). All codes track the I-front correctly, with the position never varying by more than 5 per cent from the analytical solution. These small differences are partly due to differences in our recombination rates, as discussed above, and partly a consequence of our (somewhat arbitrary) definition of the I-front position as the point of 50 per cent ionization. Our chosen parameters are such that the I-front internal structure is well resolved, and the I-front intrinsic thickness is larger than the discrepancies between the different codes. The IFT code in particular tracks the I-front almost perfectly, as is expected for this code by construction. The ray-tracing codes agree between themselves a bit better than they do with the moment-based method OTVET. This is again related to the different, somewhat more diffusive nature of the last code. The I-front velocities also show excellent agreement with the analytical result, at least until late times (at a few recombination times), at which point the I-front essentially stops and its remaining slow motion forward is not possible to resolve with the relatively coarse resolution adopted for our test. The I-front at this point is moving so slowly that most of its remaining motion takes place within a single grid cell for extended periods of time and thus falls below our resolution there.

In Fig. 8, we plot the spherically averaged radial profiles of the ionized and the neutral fraction. In the left-hand panel, we show these profiles at $t = 30$ Myr, during the early, fast expansion of the I-front. Most of the ray-tracing codes (C^2-RAY, ART, FLASH-HC and IFT) agree excellently at all radii. The OTVET, CRASH and SIMPLEX codes appear more diffusive, finding a thicker I-front transition and lower ionized fraction inside the H II region. The ZEUS code also yields lower ionized fractions inside the H II region, due to its slightly higher recombinational coefficient. The RSPH code is intermediate between the two groups of codes, finding essentially the same neutral gas profile inside the H II region as the ray-tracing codes, but a slightly thicker I-front, i.e. the ionized fraction drops more slowly ahead of the I-front.

The same differences persist in the ionized structure of the final Strömgren sphere at $t = 500$ Myr (Fig. 8, left-hand panel). The majority of the ray-tracing codes again agree fairly well. The IFT code is based on the exact analytical solution of this particular problem, and thus to a significant extent could be considered a substitute for the analytical H II region structure. Its differences from the exact solution are only close to the I-front, where the non-equilibrium effects dominate, while IFT currently assumes equilibrium chemistry. Away from the I-front, however, the ionized state of the gas is in equilibrium and there all ray-tracing codes agree perfectly. The SIMPLEX, OTVET and CRASH codes find a thicker sphere boundaries and lower ionized fractions inside, but the first two codes find a slightly smaller Strömgren sphere, while the last finds a slightly larger one. The ZEUS code finds lower ionized fractions inside the ionized region and a somewhat thicker I-front, but an overall H II region size that agrees with the other ray-tracing codes. The lower ionization is due to the current restriction of ZEUS to monochromatic RT, with its lower post-front temperatures and hence higher recombination rates.

In Fig. 9, we show histograms of the fraction of cells with a given neutral fraction during the early, fast expansion phase (at time $t =$ 10 Myr; left-hand panel), when it starts slowing down ($t = 100$ Myr, close to one recombination time; middle panel), and when the final Strömgren sphere is reached ($t = 500$ Myr; right-hand panel). These histograms reflect the differences in the I-front transition thickness and internal structure. All codes predict a transitional region of similar size, which contains a few per cent of the total volume. In

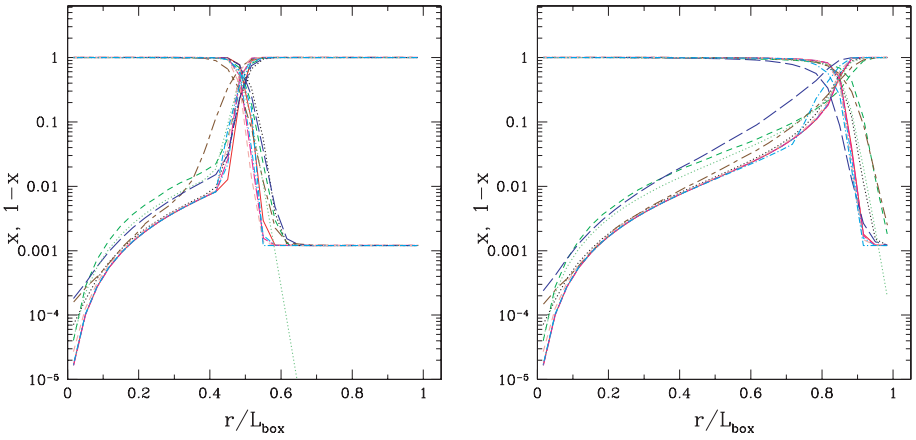

Figure 8. Test 1 (H II region expansion in uniform gas at fixed temperature): spherically averaged profiles for ionized fractions x and neutral fractions $x_{\rm H\,I} = 1 - x$ at times $t = 30$ and 500 Myr versus dimensionless radius (in units of the box size).

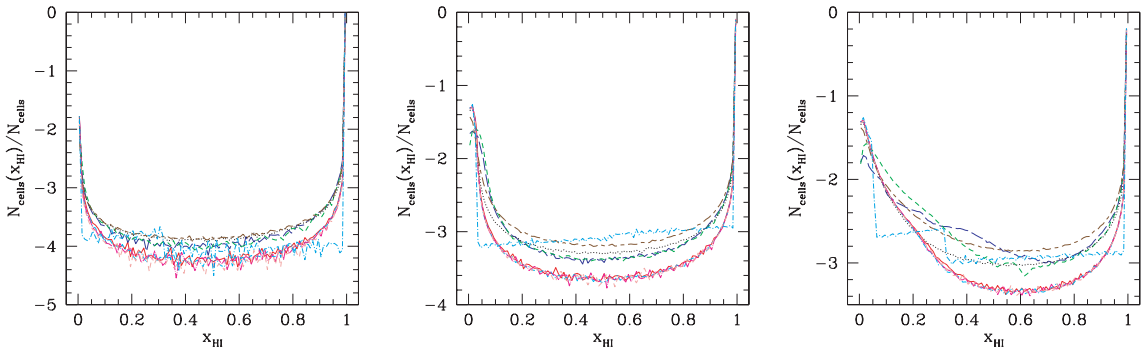

Figure 9. Test 1 (H II region expansion in a uniform gas at fixed temperature): fraction of cells with a given neutral fraction, $x_{\rm H\,I} = 1 - x$ at times $t = 10$ Myr (left-hand panel); 100 Myr (middle panel) and 500 Myr (right-hand panel).

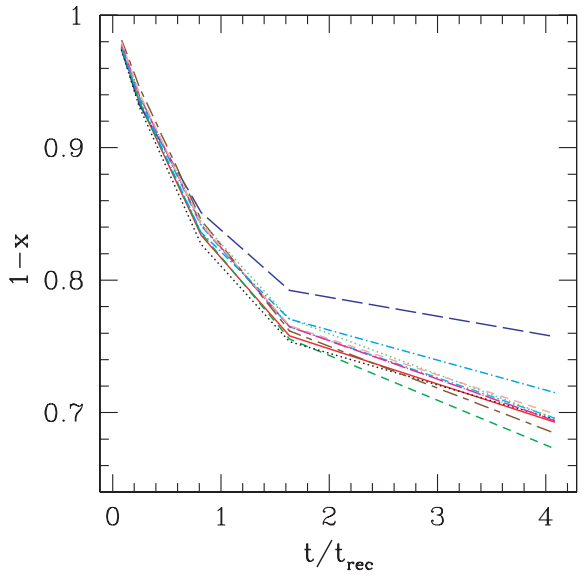

Figure 10. Test 1 (H II region expansion in a uniform gas at fixed temperature): evolution of the total neutral fraction.

detail, however, once again the results fall into two main groups. One group includes most of the ray-tracing codes, which agree perfectly at all times and predict thin I-fronts close to the analytical prediction. The other group includes the more diffusive schemes, namely OTVET, CRASH, RSPH and SIMPLEX, which all find somewhat thicker I-fronts. During the expansion phase of the H II region, these four codes agree well between themselves, but they disagree somewhat on the structure of the final equilibrium Strömgren sphere, particularly in the proximity region of the source. The IFT code histograms differ significantly from the rest, due to its assumed equilibrium chemistry, which is not quite correct at the I-front.

Finally, the evolution of the globally averaged neutral fractions is shown in Fig. 10. The same trends are evident, with the ray-tracing codes agreeing closely among themselves, while the OTVET finds about 10 per cent more neutral material at the final time, due to the different ionization structure obtained by this method.

3.3 Test 2. H II region expansion: the temperature state

Test 2 solves essentially the same problem as Test 1, but the ionizing source is assumed to have a 10^5 K blackbody spectrum and we allow the gas temperature to vary due to heating and cooling processes, as determined by the energy equation. The test geometry and gas density are the same as in Test 1. The gas is initially fully neutral and has a temperature of $T = 100$ K.

In Fig. 11, we show images of the neutral fraction on the $z = 0$ plane at time $t = 10$ Myr, during the initial fast expansion phase of the H II region. All of the results agree fairly well on the overall size of the ionized region and its internal structure. Again, there are modest differences in the thickness of the I-front and the ionizing source proximity region, e.g. the CRASH code again produces a somewhat thicker transition and smaller proximity region. The IFT code finds a significantly sharper I-front due to its equilibrium chemistry, but the internal H II region structure away from the front (which is close to equilibrium) and overall size of the ionized region both agree well with the rest of the codes. The temperature structure of the H II region, on the other hand, demonstrates significant differences (Fig. 12). These stem largely from the different way the codes handle spectral hardening, i.e. the long mean free paths of the high-energy photons due to the much lower photoionization cross-section at high frequencies. These long mean free paths result in a much thicker I-front transition and a significant pre-heating ahead of the actual I-front, since the high-energy photons heat the gas, but there are not enough of them to ionize it. The CRASH code, which follows multiple bins in frequency, finds a larger pre-heated region than the other codes. There are also significant anisotropies in the CRASH results, due to the MC sampling method used (since not many high-energy photon packets are sent, leading to undersampling in angle). In production runs, a multifrequency treatment of the single photon packets has been introduced, reducing the anisotropies in the results. The temperature results of C^2-RAY, RSPH and ART codes agree fairly well among themselves, while OTVET and FTTE give much less spectral hardening. Finally, IFT assumes that the I-front is sharp, and does not have spectral hardening by construction.

The same trends persist at later times, when the I-front is approaching the Strömgren sphere (Figs 13 and 14). Once again the H II regions predicted by all the codes are similar in size and internal structure, but with a little different I-front thickness in terms of neutral fraction and significant differences in terms of spectral hardening. The FTTE still gives a very sharp I-front, while OTVET finds somewhat less hardening, but its later time result is more similar to the other codes than at early times.

In Fig. 15, we plot the position and velocity of the I-front versus time. Unlike Test 1, in this case there is no closed-form analytical solution since the recombination coefficients vary with the spatially varying temperature. Nevertheless, as a point of reference we have again shown the analytical solution in equation (5) (assuming $T = 10^4$ K). All the codes find slightly larger H II regions and slightly

Figure 11. Test 2 (H II region expansion in a uniform gas with varying temperature): images of the H I fraction, cut through the simulation volume at coordinate $z = 0$ at time $t = 10$ Myr for (left to right and top to bottom) C^2-RAY, OTVET, CRASH, RSPH, ART, FTTE and IFT.

faster I-front propagation compared to this analytical solution. This is to be expected due to the temperature being higher than 10^4 K and the inverse temperature dependence of the recombination coefficient. The C^2-RAY, RSPH and FTTE results agree perfectly among themselves, to $\sim$1 per cent, as do the results from OTVET, ART and ZEUS, again among themselves. These two groups of results differ by $\sim$10 per cent, however, while CRASH and IFT find a H II region size intermediate between the two groups.

In Fig. 16, we show the spherically averaged radial profiles of the neutral and ionized fractions during the fast expansion phase ($t =$ 10 Myr, left-hand panel), the slowing-down phase ($t = 100$ Myr, middle panel) and the final Strömgren sphere ($t = 500$ Myr, right-hand panel). These confirm, in a more quantitative way, the trends already noted based on the 2D images above. The profiles from the C^2-RAY and RSPH codes are in excellent agreement at all radii and all times. The IFT code closely agrees with them in the source proximity region, where the gas ionized state is at equilibrium, but diverges around the I-front (due to its assumed equilibrium chemistry) and ahead of the I-front (due to its assumption that the front is sharp). Compared to these codes, the CRASH and ART find slightly higher neutral fractions close to the ionizing source, but agree well with C^2-RAY and RSPH ahead of the I-front in the spectral hardening region. The FTTE code is in excellent agreement with C^2-RAY and RSPH close to the source, but its I-front is much sharper. The OTVET code also finds a somewhat sharper I-front, but to a much lesser extent than the FTTE code, while close to the source its neutral fraction is only slightly higher than the majority of codes, and in close agreement with the ART code. Finally, the I-front derived by the ZEUS code is very sharp. This is due to the use of only single-energy photons by this code, which does not allow for spectral hardening.

The corresponding spherically averaged radial temperature profiles at the same three I-front evolutionary phases are shown in Fig. 17. All results (except the one from ZEUS, due to the monochromatic spectrum it used) agree well inside the ionized region, with the differences arising largely due to slight differences in the cooling rates adopted. The more diffusive OTVET code does not show as sharp a temperature rise in the source proximity as the other codes, but elsewhere the temperature structure it finds agrees with the majority of the codes. Again at the I-front and ahead of it the differences between the results are significant, reflecting the different handling of hard photons by the codes.

In Fig. 18, we show the histograms of the fraction of cells with a given ionized fraction x at the same times as the radial profiles shown above. During the early, fast expansion phase, all codes agree well except the OTVET code, which finds a slightly thinner I-front, but an otherwise the same histogram distribution shape, and CRASH, whose I-front is a bit thicker. IFT finds a different ionized fraction distribution, again as a consequence of its equilibrium chemistry, which is not correct at the I-front transition. Later, when the I-front slows down ($t = 100$ Myr), the same trends hold, but in addition

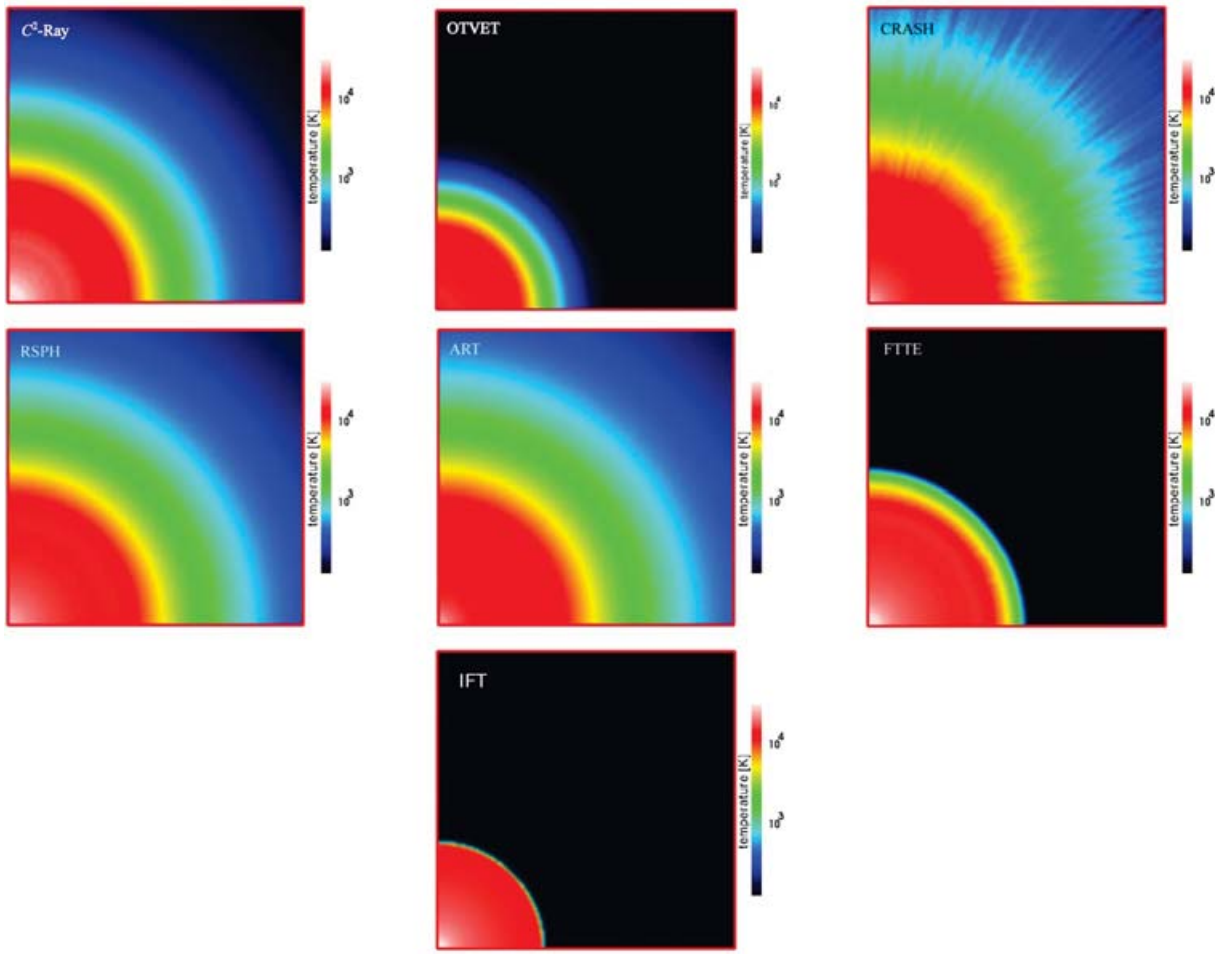

Figure 12. Test 2 (H II region expansion in a uniform gas with varying temperature): images of the temperature, cut through the simulation volume at coordinate $z = 0$ at time $t = 10$ Myr for (left to right and top to bottom) C^2-RAY, OTVET, CRASH, RSPH, ART, FTTE and IFT.

the FTTE results start diverging significantly from the rest, finding notably smaller ionized region and a quite different shape distribution in the largely neutral regions. This reflects its much sharper I-front with little spectral hardening, as noted above. Finally, the ionized fraction histogram corresponding to the Strömgren sphere ($T = 500$ Myr) shows similar differences. The C^2-RAY, ART and RSPH codes again agree very closely, and CRASH also finds a similar distribution, but with a thicker I-front and correspondingly fewer neutral cells. The OTVET distribution follows a roughly similar shape but with a thinner front transition and more neutral cells, while FTTE agrees well with the other ray-tracing codes in the highly ionized region, but still diverges considerably at the I-front and ahead of it.

The corresponding histograms of temperature are shown in Fig. 19. The ionized gas temperatures found by all codes have a strong peak at slightly above 10^4 K, with only small variations in the peak position between the different codes. This peak was to be expected, as a consequence of the combination of photoheating and hydrogen-line cooling (which peaks around 10^4 K). At higher temperatures (corresponding to cells close to the ionizing source) some differences emerge. The ray-tracing codes (C^2-RAY, CRASH, ART, RSPH, FTTE and IFT) largely agree among themselves, with only C^2-RAY finding slightly larger fraction of hot cells. OTVET, on the other hand, does not predict any cells with temperature above $\sim$16 000 K, due to missing the very hot proximity region of the source, as already noted. Below $\sim$8000 K, on the other hand, the differences between results are more significant, reflecting the variations in the I-front thickness and spectral hardening noted above. The results from CRASH, ART and RSPH agree well at all times, while the C^2-RAY histograms have similar shape, but with some offset, due to its current somewhat simplified handling of the energy input which uses a single bin in frequency. The OTVET, FTTE and IFT codes find much smaller pre-heating ahead of the I-front, and thus different distributions.

Finally, in Fig. 20 we show the evolution of the total neutral gas fraction. All codes agree well on the final neutral fraction, within $\sim$25 per cent or better. The differences are readily understood in terms of the different recombination rates, mostly as a consequence of the somewhat different temperatures found inside the H II region, in addition to the small differences in the recombination rate fits used.

3.4 Test 3. I-front trapping in a dense clump and the formation of a shadow

Test 3 examines the propagation of a plane-parallel I-front and its trapping by a dense, uniform, spherical clump. The condition for an I-front to be trapped by a clump of gas with number density $n_{\rm H}$ can be derived as follows (Shapiro et al. 2004). Let us define

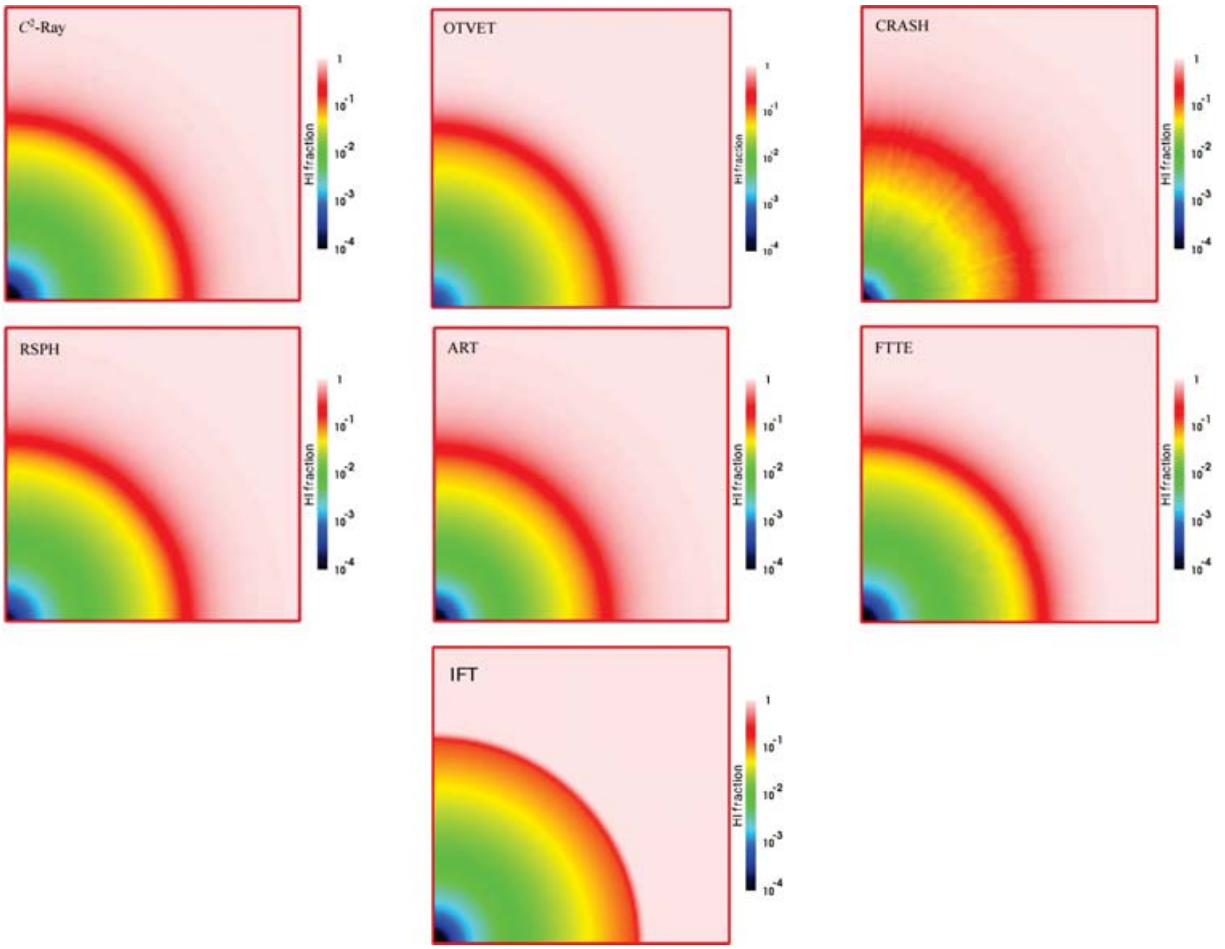

Figure 13. Test 2 (H II region expansion in a uniform gas with varying temperature): images of the H I fraction, cut through the simulation volume at coordinate $z = 0$ at time $t = 100$ Myr for (left to right and top to bottom) C^2-RAY, OTVET, CRASH, RSPH, ART, FTTE and IFT.

the Strömgren length $\ell_S(r)$ at impact parameter r from the clump centre using equation (7), but in this case following LOSs for each impact parameter. We can then define the 'Strömgren number' for the clump as $L_S \equiv 2r_{clump}/\ell_S(0)$, where r_{clump} is the clump radius and $\ell_S(0)$ is the Strömgren length at zero impact parameter. Then, if $L_S > 1$ the clump is able to trap the I-front, while if $L_S < 1$, the clump would be unable to trap the I-front and instead would be flash ionized by its passage.

For a uniform density clump, equation (7) reduces to

$$\ell_S = \frac{F}{\alpha_H^{(2)} n_H^2}, \tag{10}$$

and the Strömgren number is given by

$$L_S = \frac{2r_{clump}\alpha_B(T)n_H^2}{F}. \tag{11}$$

The numerical parameters for Test 3 are as follows. The spectrum is a blackbody with effective temperature $T_{eff} = 10^5$ K and constant ionizing photon flux, $F = 10^6$ s^{-1} cm^{-2}, incident to the $y = 0$ box side; the hydrogen number density and initial temperature of the environment are $n_{out} = 2 \times 10^{-4}$ cm^{-3} and $T_{out,init} = 8000$ K, while inside the clump they are $n_{clump} = 200n_{out} = 0.04$ cm^{-3} and $T_{clump,init} = 40$ K. The box size is $L = 6.6$ kpc, the radius of the clump is $r_{clump} = 0.8$ kpc, and its centre is at $(x_c, y_c, z_c) = (5, 3.3, 3.3)$ kpc, or $(x_c, y_c, z_c) = (97, 64, 64)$ cells; and the evolution time is 15 Myr. For these parameters and assuming for simplicity that the Case B recombination coefficient is given by $\alpha_B(T) = 2.59 \times 10^{-13}\ (T/10^4\ K)^{-3/4}$, we obtain $\ell_S \approx 0.78(T/10^4\ K)^{3/4}$ kpc and $L_S \approx 2.05(T/10^4\ K)^{-3/4}$; thus, along the axis of symmetry the I-front should be trapped approximately at the centre of the clump for $T = 10^4$ K. In reality, the temperature could be expected to be somewhat different and spatially varying, but to a rough first approximation this estimate should hold.

In fact, the I-front does get trapped as expected, slightly beyond the clump centre. In Fig. 21, we plot $(r_I - x_c)/\ell_S$, the evolution of the position of the I-front with respect to the clump centre in units of the Strömgren length (top panel) and the corresponding velocity evolution (in units of $2c_{s,I}(T = 10^4\ K) = 2(p/\rho)^{1/2}$, twice the isothermal sound speed in gas at temperature of 10^4 K), both versus $t/t_{rec,0}$, time in units of the recombination time inside the clump (which is ∼3 Myr at 10^4 K). The I-front is initially highly supersonic due to the low density outside the clump. Once it enters the clump it slows down sharply, to about 20 times the sound speed, by the same factor as the density jump at the clump boundary. As it penetrates further into the clump, it approaches its (inverse, i.e. outside-in) Strömgren radius at time $t \sim t_{rec,0}$, at which point the propagation slows down even further until the I-front is trapped after a few recombination times. The velocity drops below $2c_{s,I}$, at which point if gas motions were allowed the I-front would become slow D-type (i.e. coupled to the gas motion, rather than much faster than

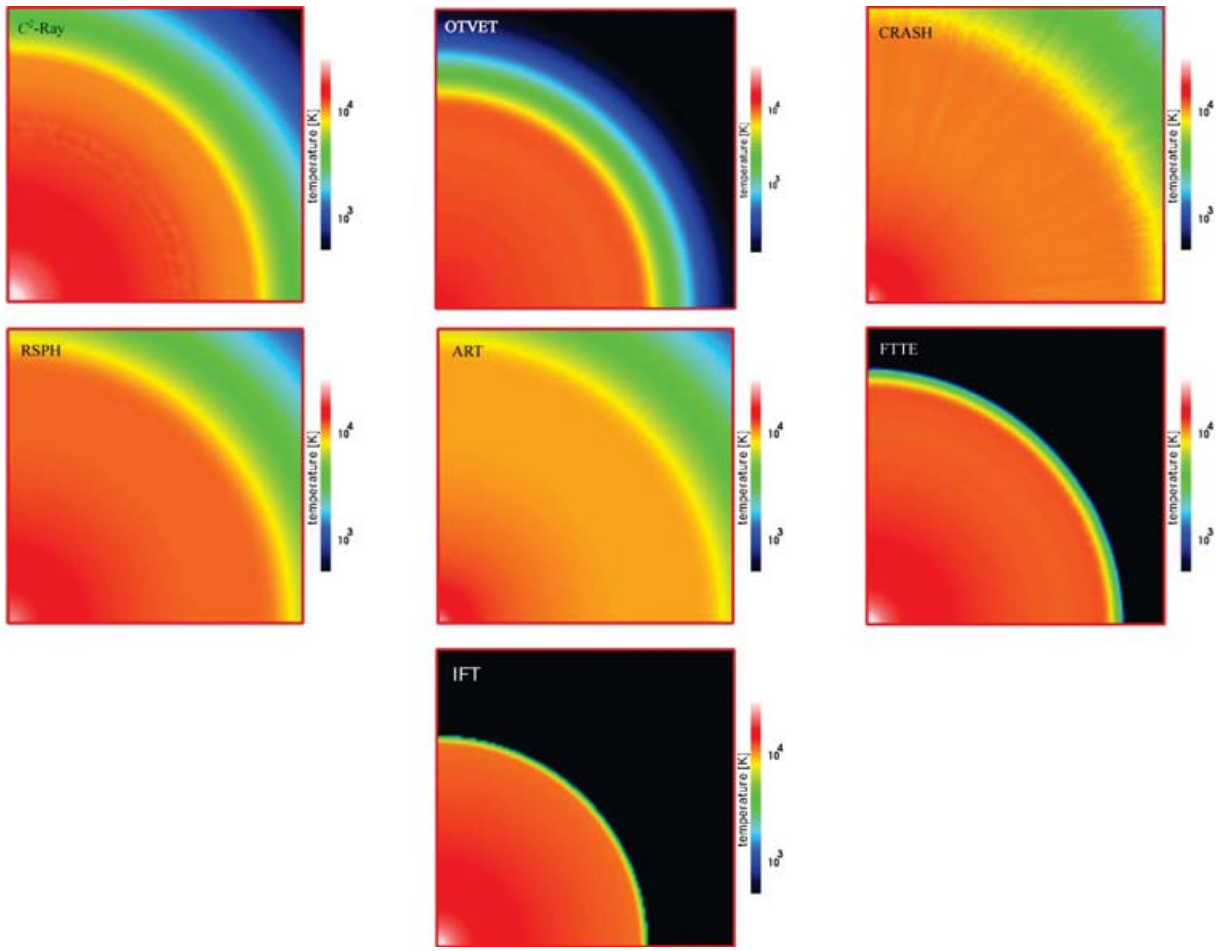

Figure 14. Test 2 (H II region expansion in a uniform gas with varying temperature): images of the temperature, cut through the simulation volume at coordinate $z = 0$ at time $t = 100$ Myr for (left to right and top to bottom) C^2-RAY, OTVET, CRASH, RSPH, ART, FTTE and IFT.

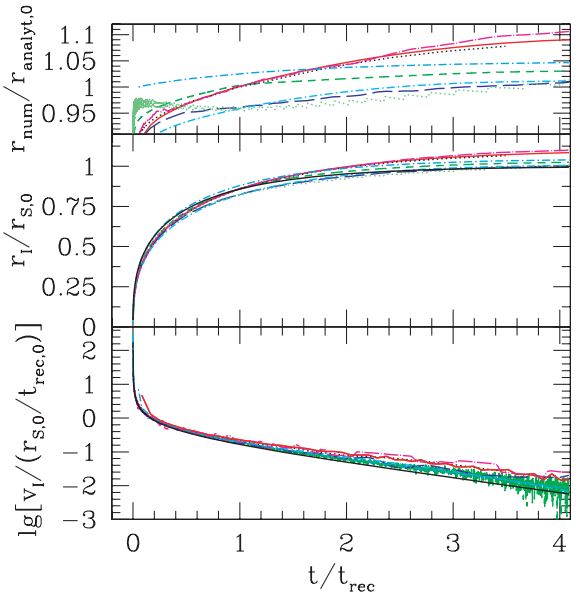

Figure 15. Test 2 (H II region expansion in a uniform gas with varying temperature): the evolution of the position and velocity of the I-front.

them). All codes capture these basic phases of the trapping process correctly and agree well on both the front position and velocity. We note here that the FLASH-HC code currently does not have the ability to track fast I-fronts, so its data start only after the front has slowed down. The IFT method assumes a sharp front, and thus does not allow pre-heating and partial ionization ahead of the front, which results in its being slowed down more abruptly than is the case for the other codes. Due to some diffusion, the RSPH code finds that the front slows down slightly before the I-front actually enters the clump. There are also minor differences in the later stages of the evolution, to be discussed in more detail below.

In Fig. 22, we show the images of the neutral gas fraction on the plane through the centre of the clump at time $t = 1$ Myr, when the I-front is already inside the clump, but still not trapped and moving supersonically. The ionizing source is far to the left of the box. All results show nice, sharp shadows behind the clump, as expected for such a dense, optically thick clump. Only the RSPH code shows diffusion at the shadow boundaries, due to the intrinsic difficulty of representing such a sharply discontinuous density distribution with SPH particles and the corresponding smoothing kernel. The FLASH-HC code yields a notably sharper I-front in both the clump and the external medium (where it is the only calculation to still have some gas with neutral fraction above $\sim 10^{-4}$). This is due to its current inability to correctly track fast I-fronts, as discussed above,

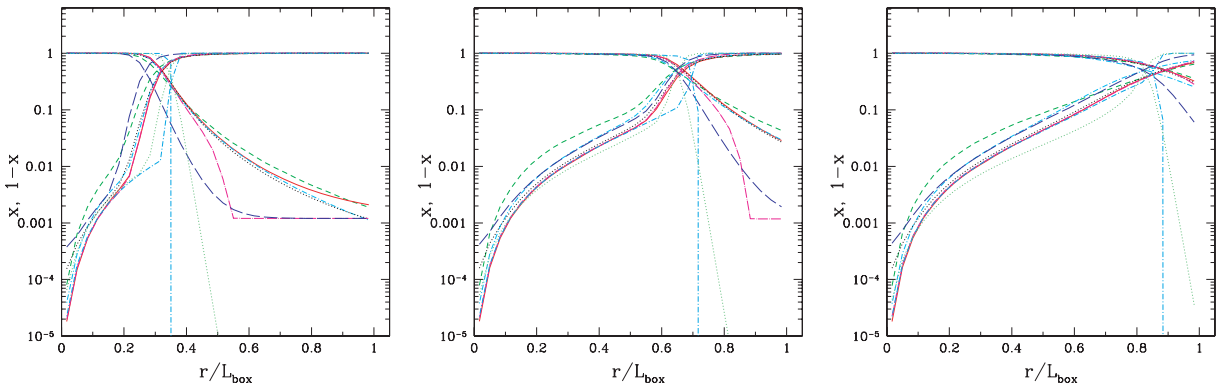

Figure 16. Test 2 (H II region expansion in a uniform gas with varying temperature): spherically averaged ionized fraction x and neutral fraction $1 - x$ profiles at times $t = 10$, 100 and 500 Myr.

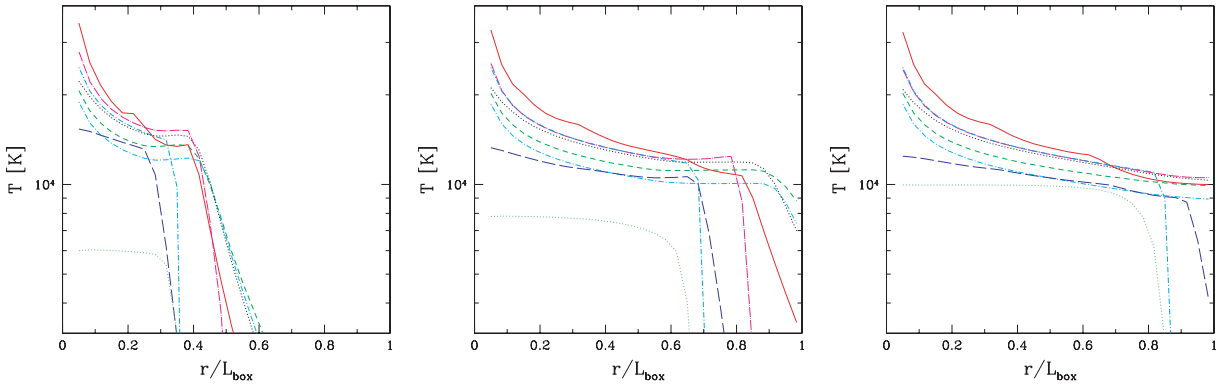

Figure 17. Test 2 (H II region expansion in a uniform gas with varying temperature): spherically averaged temperature profiles at times $t = 10$, 100 and 500 Myr (from left to right).

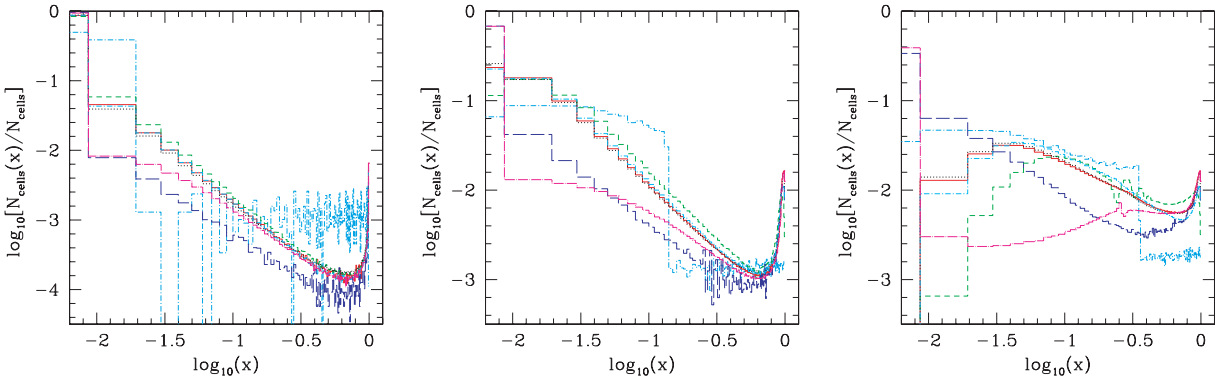

Figure 18. Test 2 (H II region expansion in a uniform gas with varying temperature): fraction of cells with a given ionized fraction, x, at times $t = 10$ Myr (left-hand panel), 100 Myr (middle panel) and 500 Myr (right-hand panel).

which leads to somewhat incorrect early evolution. The corresponding temperature image cuts (Fig. 23) show the same trends, namely that FLASH-HC and IFT find a very sharp transition, while the rest of the codes agree reasonably well, with only minor differences in the pre-heating region.

In Fig. 24, we show the images of the neutral fraction at the final time of the simulation, $t = 15$ Myr. All codes except CRASH find very similar ionized structure inside the clump. The CRASH result has significantly higher neutral fraction inside the clump, and correspondingly larger shadow behind the clump, as well as slightly higher neutral gas fraction in the low-density gas. This could be due to the fact that, as mentioned in Section 3.3, CRASH follows multiple bins in frequency over a wider frequency range with respect to the other codes; this results in a higher ionizing power at high frequencies, which also have smaller photoionization cross-sections. This in turn could be the origin of the lower ionization state of the clump and of the low-density gas. The RSPH result again exhibits significant diffusion around the edges of the shadow. The corresponding temperature structures, on the other hand (Fig. 25), show some differences, which stem from the different treatments of

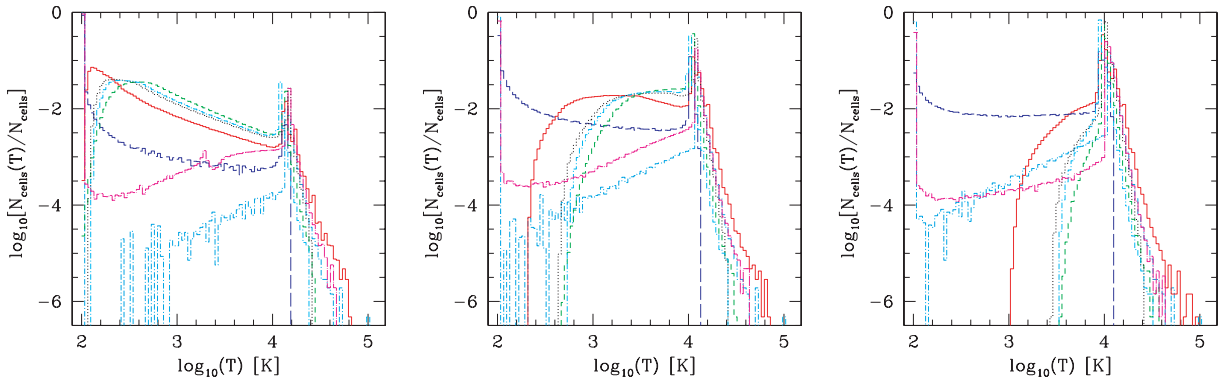

Figure 19. Test 2 (H II region expansion in a uniform gas with varying temperature): fraction of cells with a given temperature T at times $t = 10$ Myr (left-hand panel), 100 Myr (middle panel) and 500 Myr (right-hand panel).

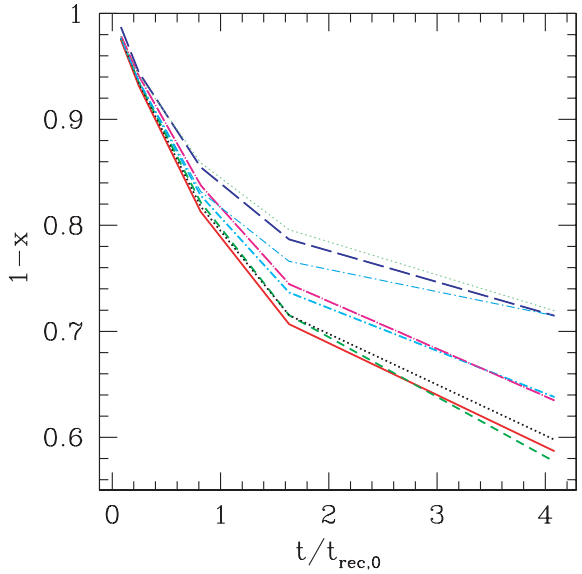

Figure 20. Test 2 (H II region expansion in a uniform gas with varying temperature): evolution of the total neutral gas fraction.

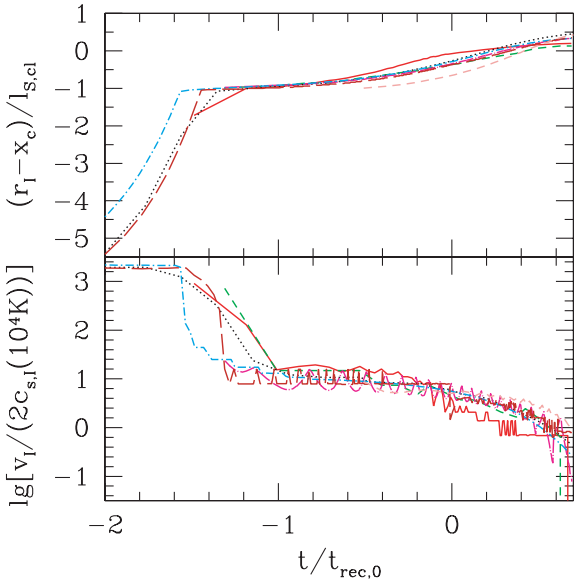

Figure 21. Test 3 (I-front trapping in dense clump): the evolution of the position and velocity of the I-front.

the energy equation and spectral hardening by the codes. The FTTE and IFT codes find almost no pre-heating in the shielded region and the shadow behind it. C^2-RAY and CRASH yield smaller self-shielded regions and some hard photons penetrating into the sides of the shadow. Finally, RSPH, FLASH-HC and CORAL find almost no gas that is completely self-shielded, but still find sufficient column densities to create temperature-stratified shadows similar to the ones found by C^2-RAY and CRASH codes, albeit at higher temperature levels. The CORAL result also has a thin, highly heated shell at the source side of the clump, resulting from this code's problems in properly finding the temperature state in the first dense, optically thick cells encountered by its rays, which leads to their overheating. In production runs, this problem was corrected by increasing the resolution and decreasing the cell size so that cells are not as optically thick, and by the gas motions, which quickly cool the gas down as it expands. The low-density gas outside the clump is somewhat cooler in the CRASH and RSPH results compared to the other codes.

These observations are confirmed by the evolutions of the mean ionized fraction and the mean temperature inside the clump, shown in Fig. 26. All codes agree very well on the evolution of the mean ionized fraction, except for CRASH, which finds ∼25 per cent lower final ionized fraction, and for FLASH-HC, which early on finds a lower ionized fraction, but catches up with the majority of the codes as the I-front becomes trapped. In terms of mean temperature, CORAL and to a lesser extent FLASH-HC find higher mean temperature due to the overheating of some cells mentioned above.

In Fig. 27, we show the ionized and neutral fraction profiles along the axis of symmetry at three stages of the evolution – early ($t = 1$ Myr), during the slow-down due to recombinations ($t = 3$ Myr, about one recombination time in the clump) and late ($t = 15$ Myr). Only the region inside and around the clump is plotted in order to show details. In the pre-ionization, spectrum-hardening zone ahead of the main I-front all profiles agree fairly well at all times, except that the IFT profiles have a sharp I-front and no hardening by definition, and the FTTE current method appears to produce no hardening, either. Otherwise, these two codes agree well with the others in the post-front region. Some differences emerge in the position of the I-front (defined as the point of 50 per cent ionized fraction) and the neutral fraction profiles behind the I-front. During the initial, fast propagation phase of the front all codes agree on its position. However,

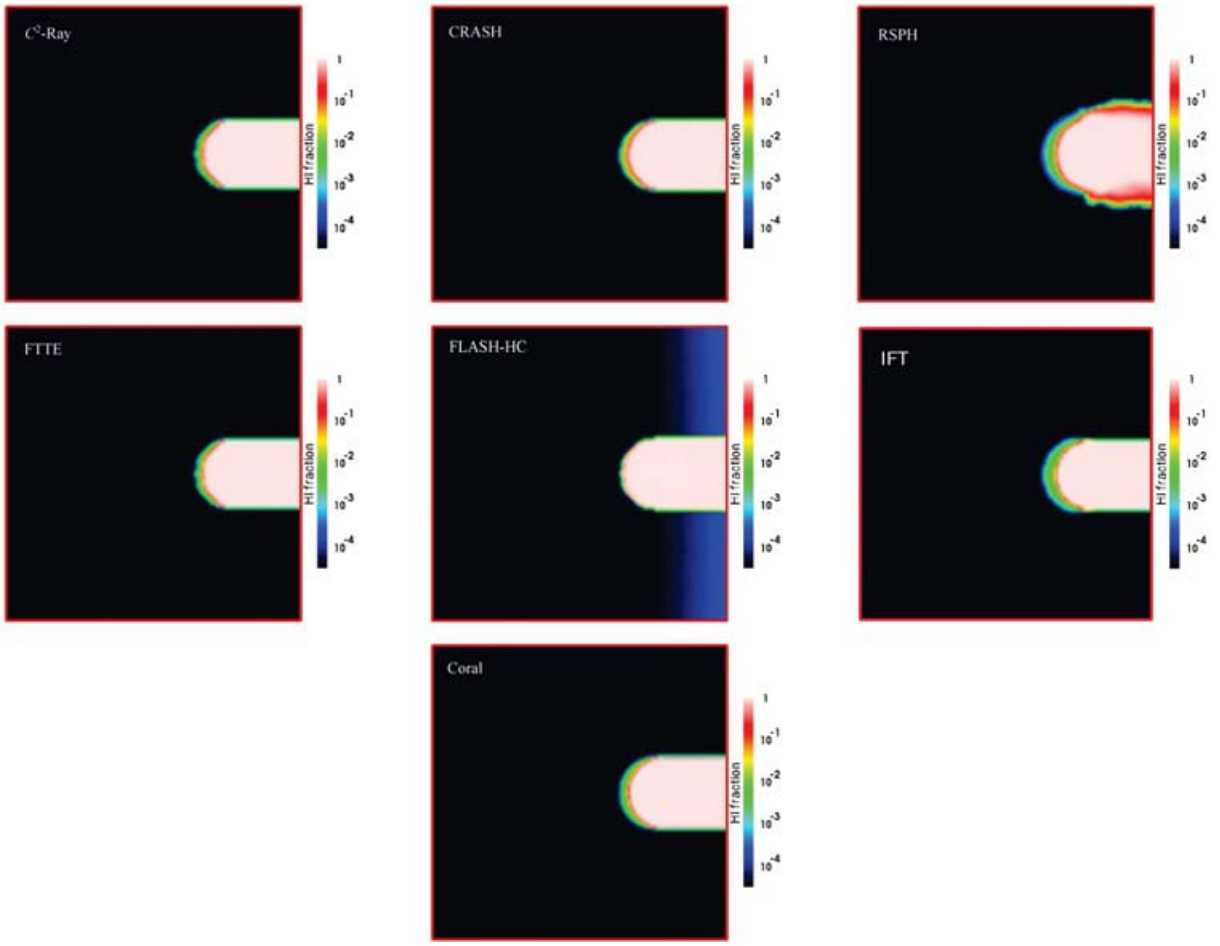

Figure 22. Test 3 (I-front trapping in dense clump): images of the H I fraction, cut through the simulation volume at mid-plane at time $t = 1$ Myr for C^2-RAY, CRASH, RSPH, FTTE, FLASH-HC, IFT and CORAL.

CRASH and, to a lesser extent, FLASH-HC both find consistently higher neutral fractions in the ionized part of the clump than the rest of the codes. As a consequence, they show that the I-front is trapped closer to the surface of the dense clump. The reason for this could be seen in the corresponding temperature profiles (Fig. 28). Both CRASH and FLASH-HC obtain a slightly lower temperature for the dense ionized gas, resulting in a higher recombination rate there. The RSPH and IFT results show some diffusion at the source-side clump boundary (at $r/L_{\rm box} \sim 0.64$), resulting in a slightly less sharp transition there, regardless of the sharp discontinuity of the gas density. The temperatures in the post-front fraction of the clump otherwise agree quite well, with the exception of the first cells on the source side, where CORAL finds very high temperatures, as was already mentioned. In the pre-front region, the temperature profile results also agree fairly well. Only IFT and FTTE differ there, again yielding a very sharp I-front. C^2-RAY finds a bit less pre-heating in this region, due to its single frequency bin method. Until $t = 3$ Myr, all results except the FLASH-HC one agree that the shadow region right behind the clump is completely shielded and remains at the initial temperature (8000 K). At the final time, however, more differences emerge. At this time only IFT and FTTE still find no pre-heating, and C^2-RAY and CRASH find only little heating of the shadow. The CORAL, RSPH and FLASH-HC results all find significant pre-heating, albeit at different levels. RSPH is the only code that at the final time finds no partially shielded gas at the back of the clump, the presence of which is indicated by the temperature dip at $r/L_{\rm box} \sim 0.88$ for all the other results.

The final results we show for this test are histograms of the fraction of cells inside the clump with a given ionized fraction (Fig. 29) and with a given temperature (Fig. 30) at the same three evolutionary stages discussed above. These histograms reflect the differences in the thickness and the internal structure of the I-fronts inside the clump. During the initial fast propagation and the slowdown phases, the RSPH and CORAL codes consistently find somewhat thicker I-front transitions than the other codes. The results of C^2-RAY, CRASH and FLASH-HC start with the front somewhat thinner than the ones for RSPH and CORAL, but the distribution changes as the I-front gets trapped. At the final time, the ionized fraction distributions are very similar, with only the one for CRASH being slightly thicker. Finally, FTTE and IFT find significantly thinner front transitions and significant self-shielded gas fractions, as was noted before. The corresponding temperature distributions all show a strong peak at a similar temperature, a few tens of thousands of degrees, typical for gas heated by photoionization. This temperature is well above 10^4 K because of the hot blackbody spectrum of the source. At temperatures lower than this peak value, which largely correspond to the pre-heated zone ahead of the I-front, there again is broad agreement, apart from the FTTE and IFT codes which have a sharp front and little pre-heating. At the high-temperature end of the distribution, C^2-RAY, FTTE, FLASH-HC and CORAL diverge from the rest, by finding a small

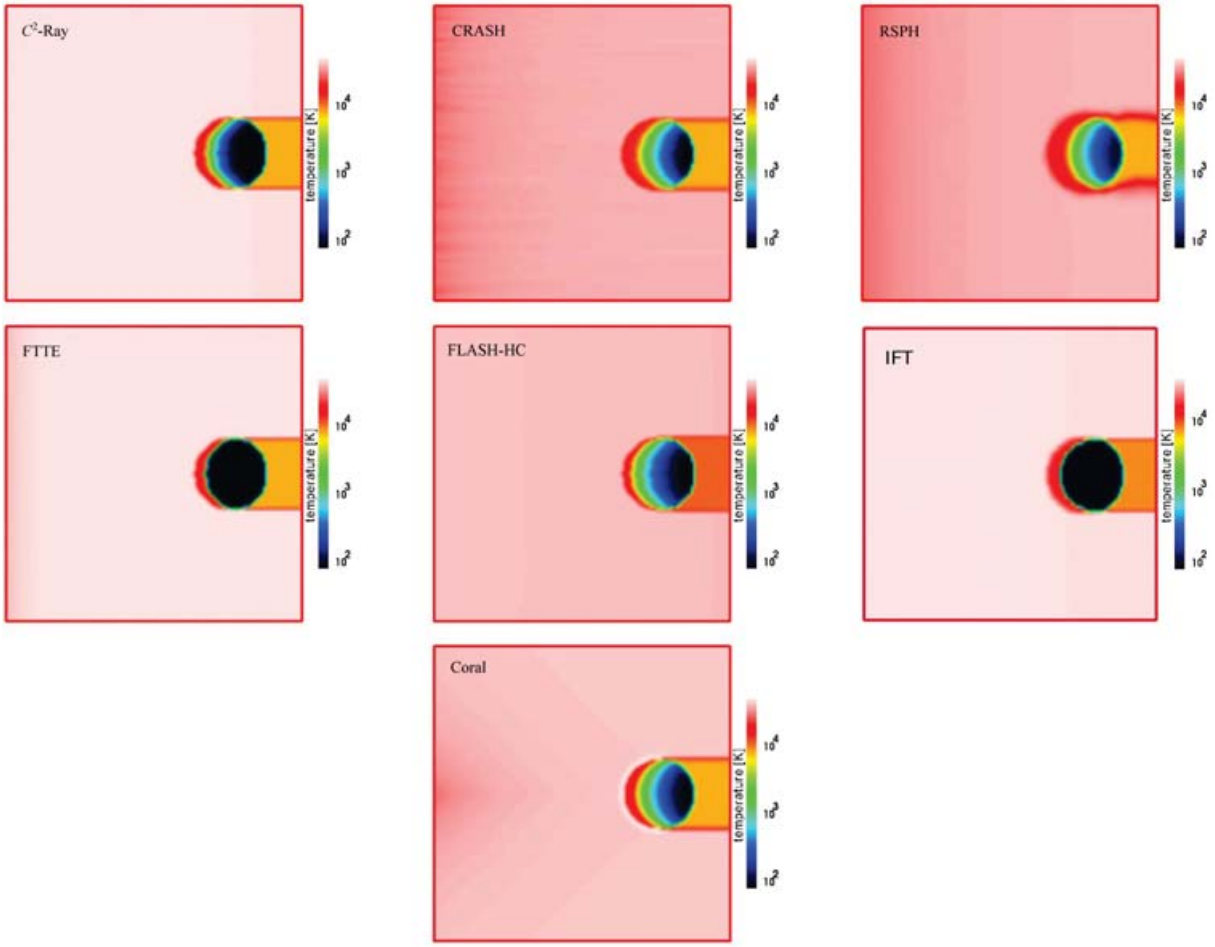

Figure 23. Test 3 (I-front trapping in dense clump): images of the temperature, cut through the simulation volume at mid-plane at time $t = 1$ Myr for C^2-RAY, CRASH, RSPH, FTTE, FLASH-HC, IFT and CORAL.

fraction of very hot cells, while the majority of codes find essentially no cells hotter than the distribution peak. It should be noted, however, that the fraction of these cells is only 0.1–1 per cent of the total.

3.5 Test 4. Multiple sources in a cosmological density field

Test 4 involves the propagation of I-fronts from multiple sources in a static cosmological density field. The initial condition is provided by a time-slice (at redshift $z = 9$) from a cosmological N-body and gasdynamic simulation performed using the cosmological PM+TVD code by D. Ryu (Ryu et al. 1993). The simulation box size is 0.5 h^{-1} comoving Mpc, the resolution is 128^3 cells, 2×64^3 particles. The haloes in the simulation box were found using a friends-of-friends halo finder with linking length of 0.25. For simplicity, the initial temperature is fixed at $T = 100$ K everywhere. The ionizing sources are chosen so as to correspond to the 16 most massive haloes in the box. We assume that these have a blackbody spectrum with effective temperature $T_{\rm eff} = 10^5$ K. The ionizing photon production rate for each source is constant and is assigned assuming that each source lives $t_{\rm s} = 3$ Myr and emits $f_\gamma = 250$ ionizing photons per atom during its lifetime. Hence,

$$\dot{N}_\gamma = f_\gamma \frac{M\Omega_{\rm b}}{\Omega_0 m_p t_{\rm s}}, \qquad (12)$$

where M is the total halo mass, $\Omega_0 = 0.27$, $\Omega_{\rm b} = 0.043$ and $h = 0.7$.

For simplicity, all sources are assumed to switch on at the same time. The boundary conditions are transmissive (i.e. photons leaving the computational box are lost, rather than coming back in as in periodic boundary conditions). The evolution time is $t = 0.4$ Myr.

In Fig. 31, we show slices of the H I fraction cut through the simulation box at coordinate $z = z_{\rm box}/2$ and time $t = 0.05$ Myr, and in Fig. 32 we show the corresponding temperature distributions at the same time. SIMPLEX does not appear in the temperature maps, since currently the code does not follow the temperature evolution self-consistently, but instead assumes a constant temperature. Figs 33 and 34 show the same as above but at time $t = 0.2$ Myr. Some discrepancies are already evident from a visual inspection, which shows somewhat different morphologies, but still general agreement. In Fig. 35 (left-hand panel), we present the temporal evolution of the volume- (thin lines) and mass-weighted (thick lines) ionized fractions. While CRASH and FTTE find comparable ionized fractions, C^2-RAY and SIMPLEX produce slightly higher and lower values, respectively. The lower value in SIMPLEX is obtained as a consequence of the temperature being fixed to 10^4 K, which is a little lower than that obtained by the other codes, resulting in a higher recombination rate.

The finer sampling in CRASH of the high-energy tail of the spectrum allows a higher resolution of its hardening. As the total energy is distributed differently from the other codes (more energy is in

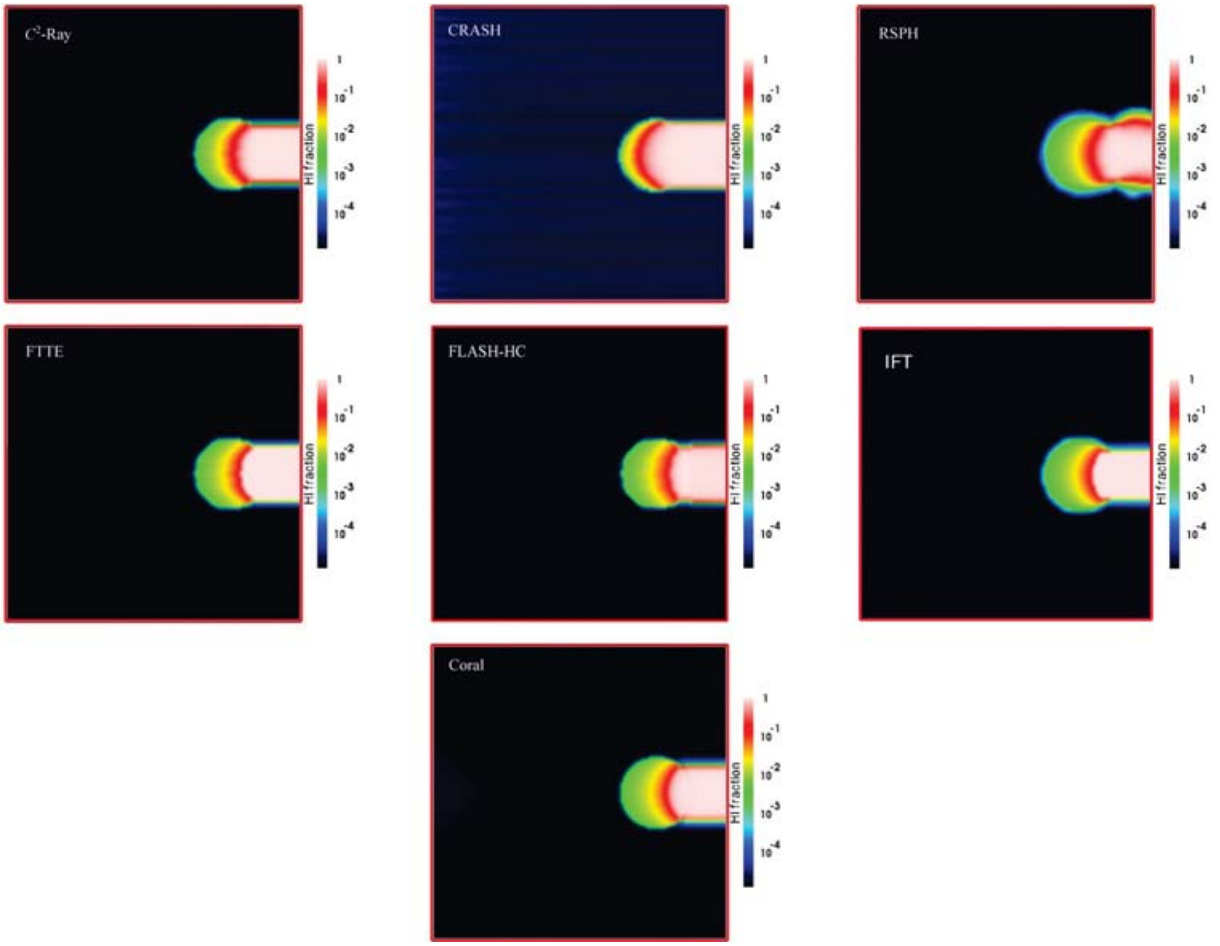

Figure 24. Test 3 (I-front trapping in dense clump): images of the H I fraction, cut through the simulation volume at mid-plane at time $t = 15$ Myr for C^2-RAY, CRASH, RSPH, FTTE, FLASH-HC, IFT and CORAL.

the hard photons), this results in less ionization/heating closer to the sources, more ionization/heating further away and a lower mean ionized fraction.

In Figs 36 and 37, we show histograms of the ionized fraction and the temperature at times $t = 0.05$, 0.2 and 0.4 Myr. While C^2-RAY and FTTE agree quite well, especially at later times, CRASH, as explained above, produces a thicker I-front transition. The thickness of the I-front as found by SIMPLEX appears to oscillate with time, initially starting thick, then becoming thinner, and thick again towards the end of the simulation. This might have been caused by the interpolation of its unstructured grid to the regular grid required for the results. In terms of temperature, CRASH finds a systematically lower peak ($\sim 1.6 \times 10^4$ K, compared to $\sim 6.3 \times 10^4$ K for C^2-RAY and FTTE, which agree well there) inside the ionized regions and a higher value in the lower density regions. This is once again due to the spectrum hardening effects discussed above. The peak produced by FTTE at very low temperatures arises because of the lack of spectral hardening and sharp I-fronts consistently produced by this code, in which case no photons propagate ahead of the I-front and thus the gas away from the sources remains cold and neutral.

To understand whether the differences discussed above can in fact be attributed to photon hardening and the different treatment of the high-energy tail of the spectrum, we have repeated the same simulations with a softer blackbody spectrum with effective temperature $T_{\rm eff} = 3 \times 10^4$ K, in which case the spectral hardening and I-front spreading should be minimized. We note that this part was not done by the SIMPLEX code since currently it does not treat different spectra. Our results are shown in Fig. 35 (right-hand panel), as well as Figs 38 and 39. The averaged ionized fraction produced by C^2-RAY and CRASH now show a much better agreement, as far fewer hard photons are present. However, FTTE still produces a lower value, although by only $\sim$5 per cent. CRASH still gives a somewhat thicker ionizing front, due to the inherent adopted method, but the agreement is now better, especially at later times, as high-energy photons are not present in this case. This is even more evident from an analysis of the temperature behaviour, where the agreement between C^2-RAY and CRASH is now very good at all times, while FTTE consistently finds higher temperatures inside the ionized regions. These higher temperatures seem to contradict the lower ionized fractions found by this code, while the recombination rate used by this code is consistent with the others, indicating a possible (modest) problem with photon conservation.

4 SUMMARY AND CONCLUSIONS

We have presented a detailed comparison of a large set of cosmological RT methods on several common tests. The participating codes represent the full variety of existing approaches, multiple ray tracing and one moment method, which solve the RT on regular, adaptive or unstructured grids, or even with no grid at all, but instead using

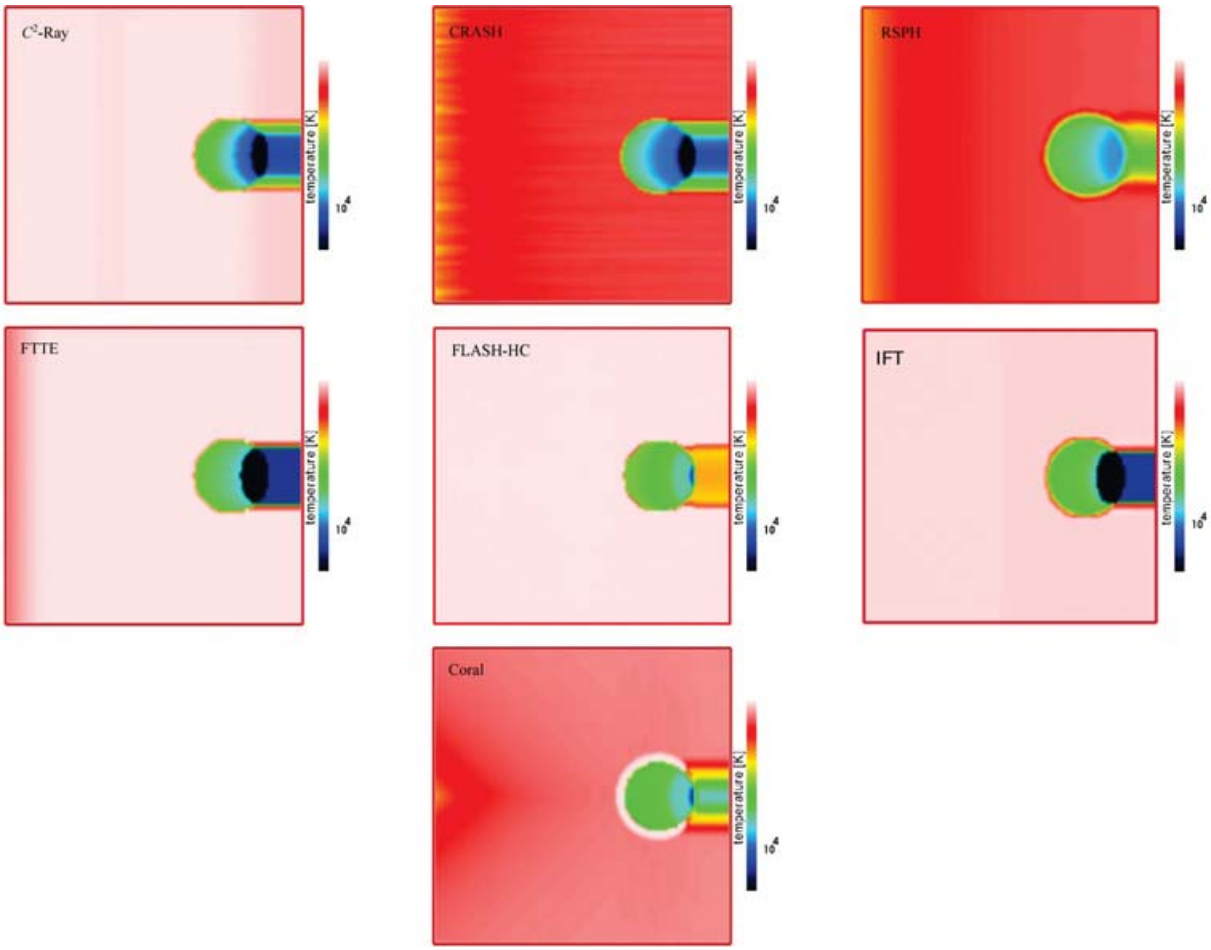

Figure 25. Test 3 (I-front trapping in dense clump): images of the temperature, cut through the simulation volume at mid-plane at time $t = 15$ Myr for C^2-RAY, CRASH, RSPH, FTTE, FLASH-HC, IFT and CORAL.

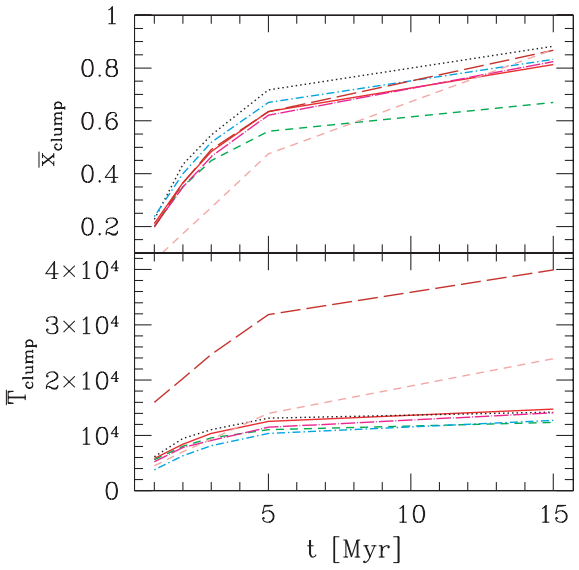

Figure 26. Test 3 (I-front trapping in dense clump): the evolution of the ionized fraction (top panel) and the mean temperature (bottom panel) inside the dense clump.

particles to represent the density field. This comparison is a collaborative project involving a large number of the cosmological RT researchers and most of the existing codes. The results from this comparison will be publicly available for testing of future codes during their development.

We began by comparing our basic physics, like chemistry, cooling rates and photoionization cross-sections, which came from a variety of sources, and evaluated the effects these have on the propagation of I-fronts. We concluded that even quite approximate rates generally result in relatively modest divergences in the results. The discrepancies were limited to ∼5 per cent in I-front position but were somewhat larger in velocity and the internal structure of the H II region (but never exceeding 20–40 per cent, and usually much smaller).

Then, we turned to some simple, but instructive and cosmologically interesting problems which tested the different aspects encountered in realistic applications. The results showed that at fixed temperature and for a monochromatic-ionizing spectrum (Test 1) all of these methods track I-fronts well, to within a few per cent accuracy, demonstrating that all codes conserve photons at that level and for this problem. There are, however, some differences in the inherent thickness (due to finite mean free path) and the internal structure of the I-fronts, related to some intrinsic diffusivity of some of the methods (OTVET, CRASH and SIMPLEX). The ray-tracing methods,

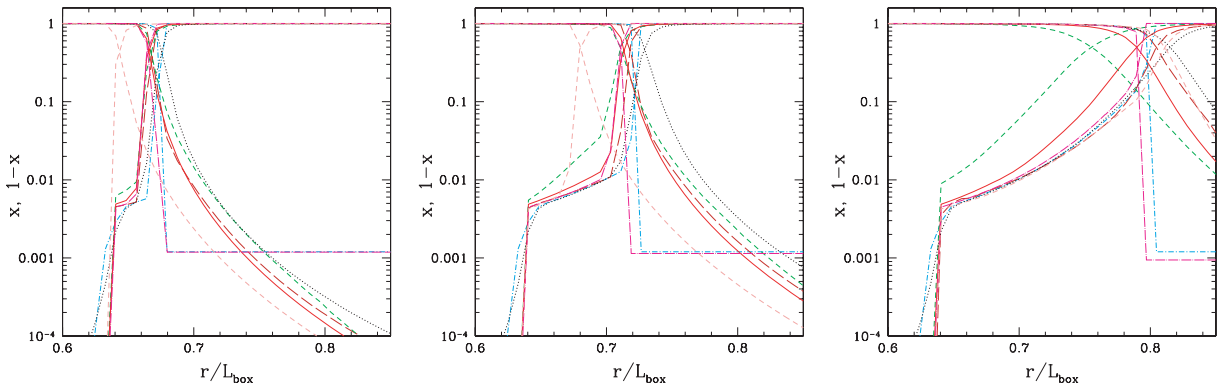

Figure 27. Test 3 (I-front trapping in dense clump): line cuts of the ionized and neutral fraction along the axis of symmetry through the centre of the clump at times $t = 1$, 3 and 15 Myr (left to right).

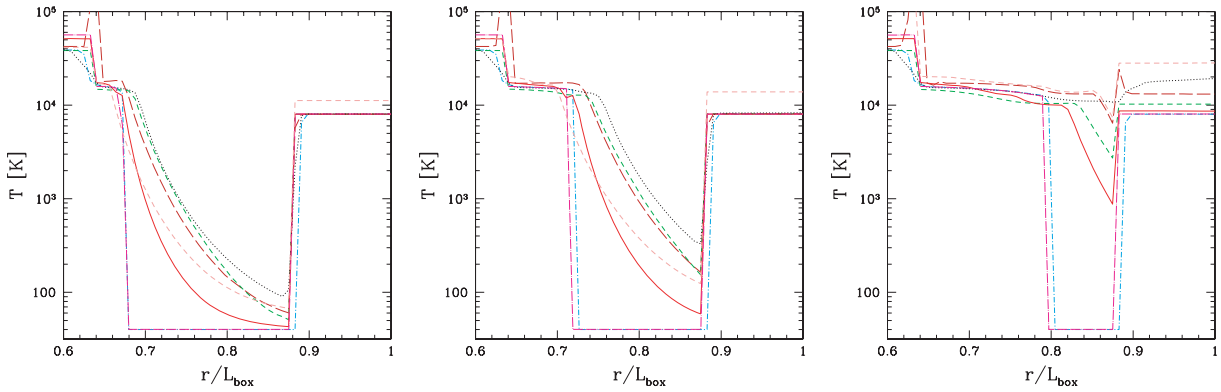

Figure 28. Test 3 (I-front trapping in dense clump): line cuts of the temperature along the axis of symmetry through the centre of the clump at times $t = 1$, 3 and 15 Myr (left to right).

on the other hand yielded transition thicknesses which were very close to the exact one. The source proximity regions are accordingly smaller for the more diffusive schemes. Some codes (CRASH and SIMPLEX) also showed notable (and for this spherically symmetric problem, unphysical) spatial anisotropies, which are probably due to insufficient sampling in photon packets and points in space, respectively.

Somewhat greater differences emerge when the temperature is allowed to vary (Test 2), although even in this case the agreement is very good, typically within 10–20 per cent in the ionized fraction. Other variations between the results are due to the variety of multifrequency RT methods and consequent spectral hardening and pre-heating ahead of the I-fronts. Some of the algorithms (FTTE, and to a much lesser extent OTVET) consistently find quite sharp I-fronts, with little spectral hardening and pre-heating, while the majority of the codes handle these features more precisely and in reasonable agreement among themselves. The IFT results are notably different since by construction it assumes sharp I-fronts and equilibrium chemistry, both of which are not very good assumptions for this particular problem. The CRASH results are also different from the other codes in the region well ahead of the I-front, which is a consequence of this code's more precise tracking of the multifrequency photon transport, which yields hard photons penetrating much deeper in the neutral gas. The same code also shows, once again, significant (and for this problem, incorrect) anisotropies due to insufficient sampling of space with photon packets.

Test 3 (I-front trapping by a dense gas clump) proved to be a fairly difficult problem, due to the sharp density discontinuity. The test involved both fast (outside the clump) and slow (inside) I-front propagation, as well as I-front trapping, casting of a shadow, and spectral hardening. Accordingly, there are notable differences between the codes in terms of the I-front trapping and its thickness inside the clump. None the less, the majority of the results agree reasonably well, and all codes produce nice, clearly defined shadows behind the dense clump. The only exception is RSPH, due to the intrinsic difficulty of representing very sharp density discontinuities with SPH particles. This problem makes the clump somewhat fuzzier, and the shadow less sharp, but the basic features still agree with the other codes. The FTTE code again finds quite sharp I-front with little spectral hardening. The FLASH-HC in its current version does not track properly fast I-fronts, and both it and CORAL yield a (unphysical) thin and very hot shell at the clump boundary. Both of these problems are related to difficulties in handling very optically thick cells by these (very similar to each other) RT methods. None the less, the mean ionized gas fraction in the clump and the I-front ionization and temperature profiles in these cases still match the other results quite well.

Finally, Test 4 studied the ionization of a cosmological density field by multiple (but a small number of) ionizing sources. The overall morphology of the H II regions showed good agreement at all times, and the evolution of the global ionized fractions agreed within ∼10 per cent, as well. The main differences once again were

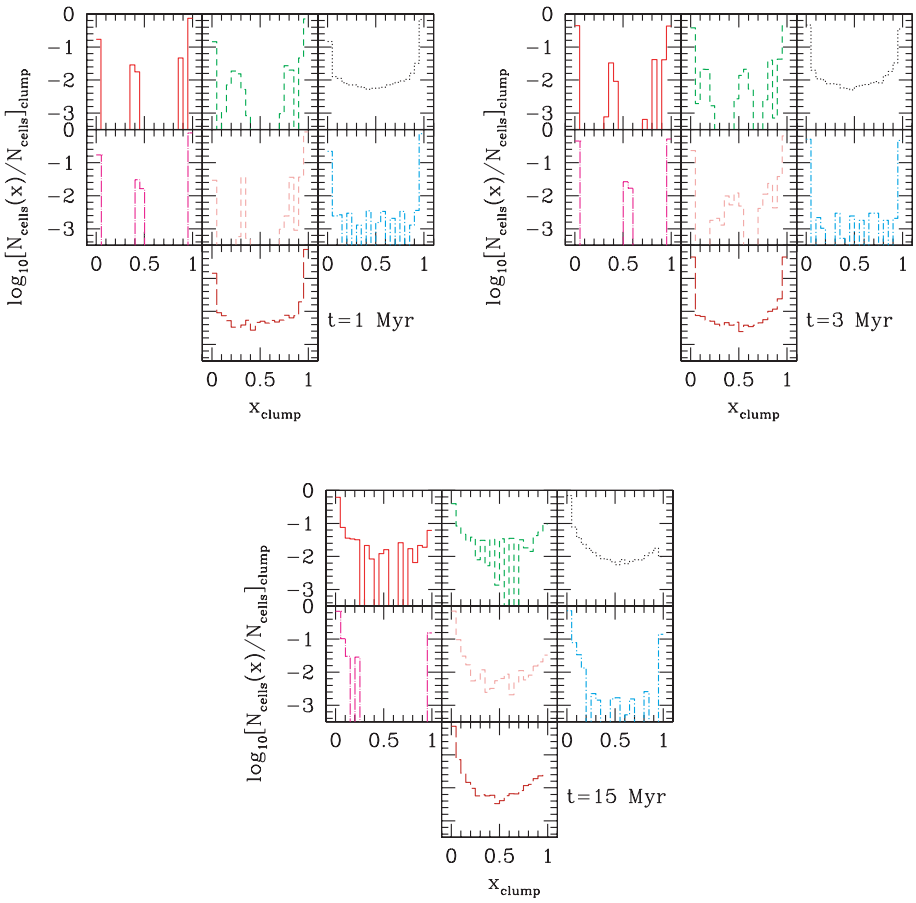

Figure 29. Test 3 (I-front trapping in dense clump): histograms of the ionized fraction inside the clump at times $t = 1$, 3 and 15 Myr.

due to the different handling of the multifrequency photon transport and the temperature equation. Due to the small simulation volume and relatively hard spectra, the I-fronts are wide and resolved in the simulations. CRASH uses many frequency bins, and thus yields more pre-heating of the neutral regions by hard photons and less hot ionized regions, while FTTE yields very little pre-heating and fairly sharp I-fronts. C^2-RAY is intermediate between the two, with significant pre-heating of the neutral regions, though somewhat less than what CRASH found, and H II regions with similar ionization levels and temperatures to the FTTE results. A follow-up run with same source luminosities, but assuming softer spectra yielded results which showed significantly reduced differences between the codes, especially between CRASH and C^2-RAY.

We conclude that the various approximations employed by the different methods perform quite well and generally produce consistent and reliable results. There are, however, certain differences between the available methods and the most appropriate method for any particular problem would vary. Therefore, the code employed should be chosen with care depending on the specific questions whose answer is sought. For example, for problems where the I-front width and spectral hardening matters significantly, attention should be paid to the accurate multifrequency treatment and the energy equation. Examples of such problems include the pre-heating of the IGM by hard photons and X-rays, and generally, obtaining the temperature state of the IGM before, during and after reionization, minihalo photoevaporation during reionization, and feedback from the first stars on nearby structures On the other hand, in problems in which the I-front structure is not resolved (due to coarse simulation resolution compared to the characteristic front width), most methods considered here should perform well and the main criterion should be their numerical efficiency. This is the case in e.g. large-scale simulations of reionization, in which case the resolution is insufficient to see the internal structure of the propagating I-fronts.

The question of the efficiency of the different codes is a very important one. It was not discussed in this paper, for several reasons. The main one of these is that, in order for the comparison project to be most inclusive, we only consider relatively simple problems, with only one or a few ionizing sources and modestly sized grids. The computational expenses of the ray-tracing codes generally scale up roughly proportionally to the number of sources, while for other methods (OTVET and SIMPLEX) they are independent of the number of sources. Thus, tests with only a few sources present would skew the efficiency comparisons heavily in favour of the ray-tracing methods. The 1D and 2D codes are also not directly comparable with the rest. There are also some issues with particular codes, e.g. OTVET is inherently periodic, thus in order to run the (non-periodic) test problems here all runs had to be performed at double box size and double the spatial resolution of the other codes; it is difficult to compare on the same footing methods which use regular grids (fixed or adaptive) with methods using unstructured grids (SIMPLEX) or particles (RSPH). Proper assessment of the computational efficiency of the variety of methods presented here would require a different set of tests, carefully constructed to measure

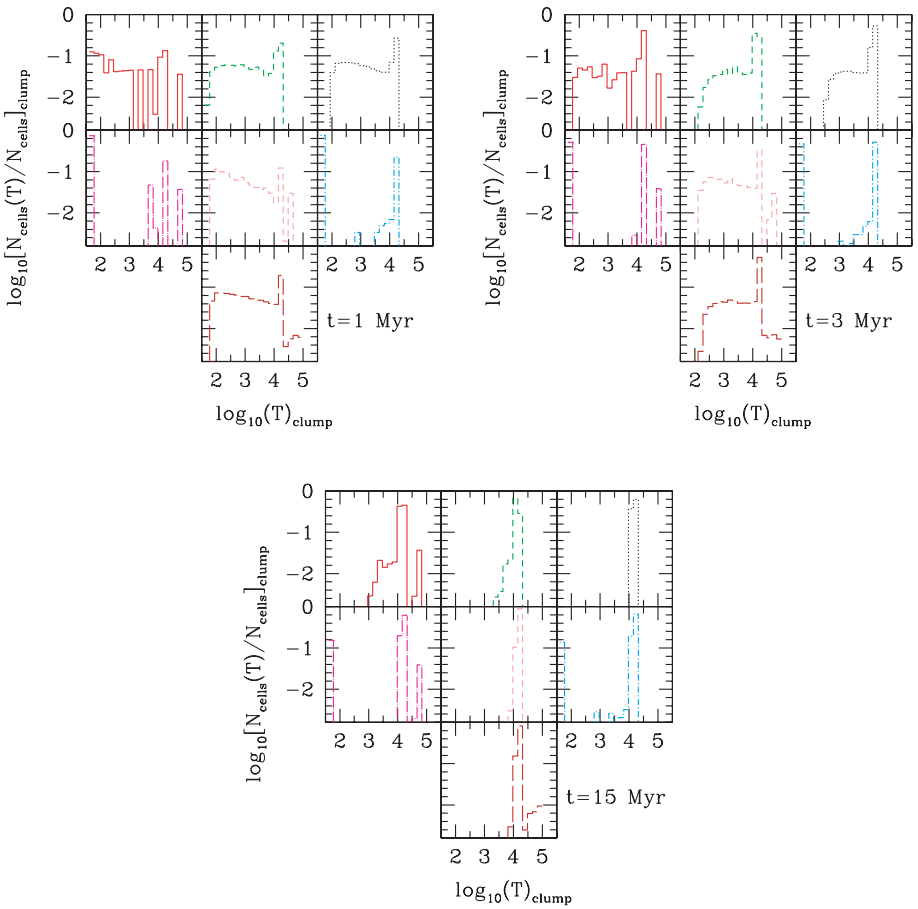

Figure 30. Test 3 (I-front trapping in dense clump): histograms of the temperature inside the clump at times $t = 1$, 3 and 15 Myr.

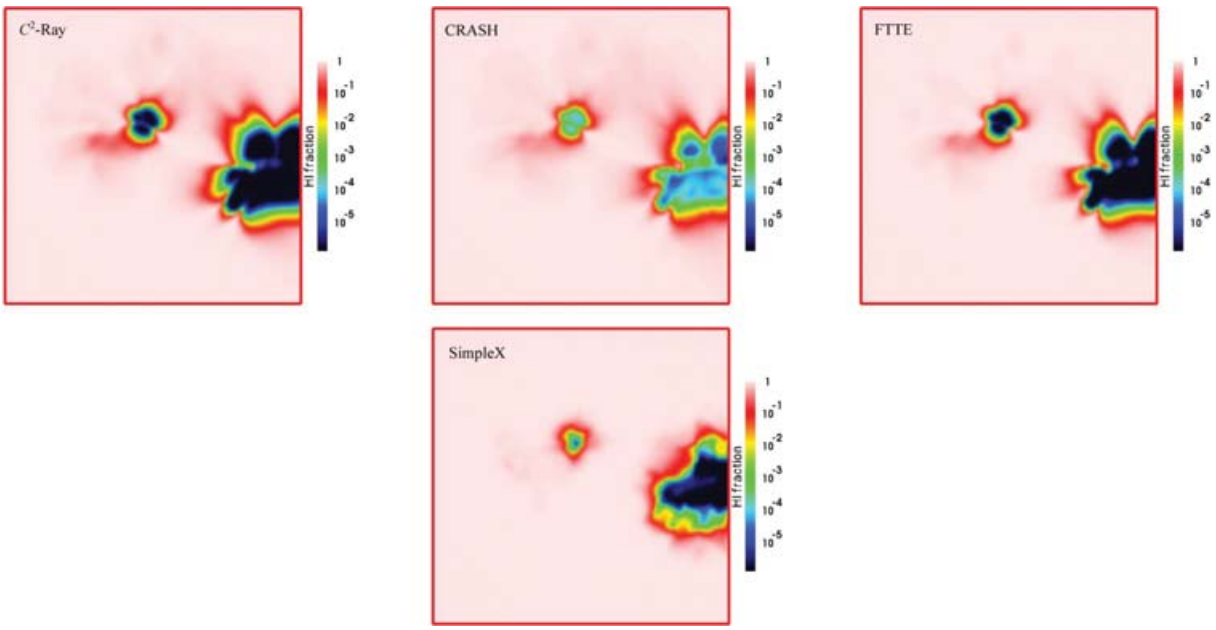

Figure 31. Test 4 (reionization of a cosmological density field): images of the H I fraction, cut through the simulation volume at coordinate $z = z_{\rm box}/2$ and time $t = 0.05$ Myr for C^2-RAY (left-hand panel), CRASH (middle panel), FTTE (right-hand panel) and SIMPLEX (bottom panel). The blackbody spectrum has an effective temperature $T_{\rm eff} = 10^5$ K.

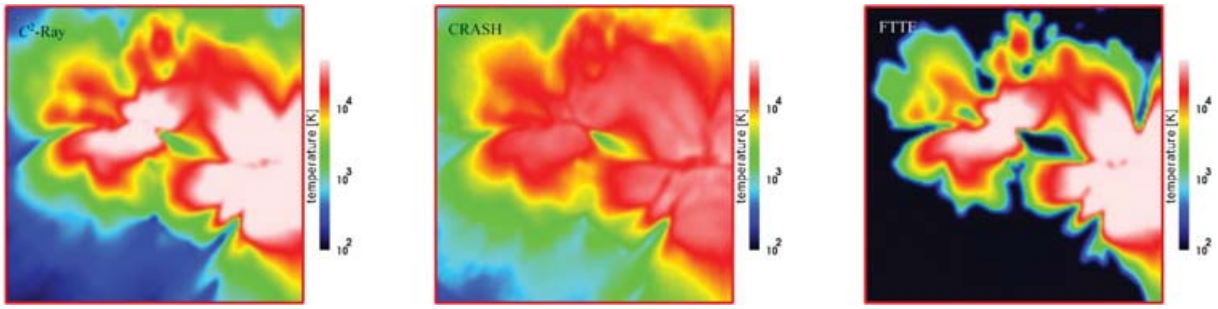

Figure 32. Test 4 (reionization of a cosmological density field): images of the temperature, cut through the simulation volume at coordinate $z = z_{\rm box}/2$ and time $t = 0.05$ Myr for C^2-RAY (left-hand panel), CRASH (middle panel) and FTTE (right-hand panel). The blackbody spectrum has an effective temperature $T_{\rm eff} = 10^5$ K.

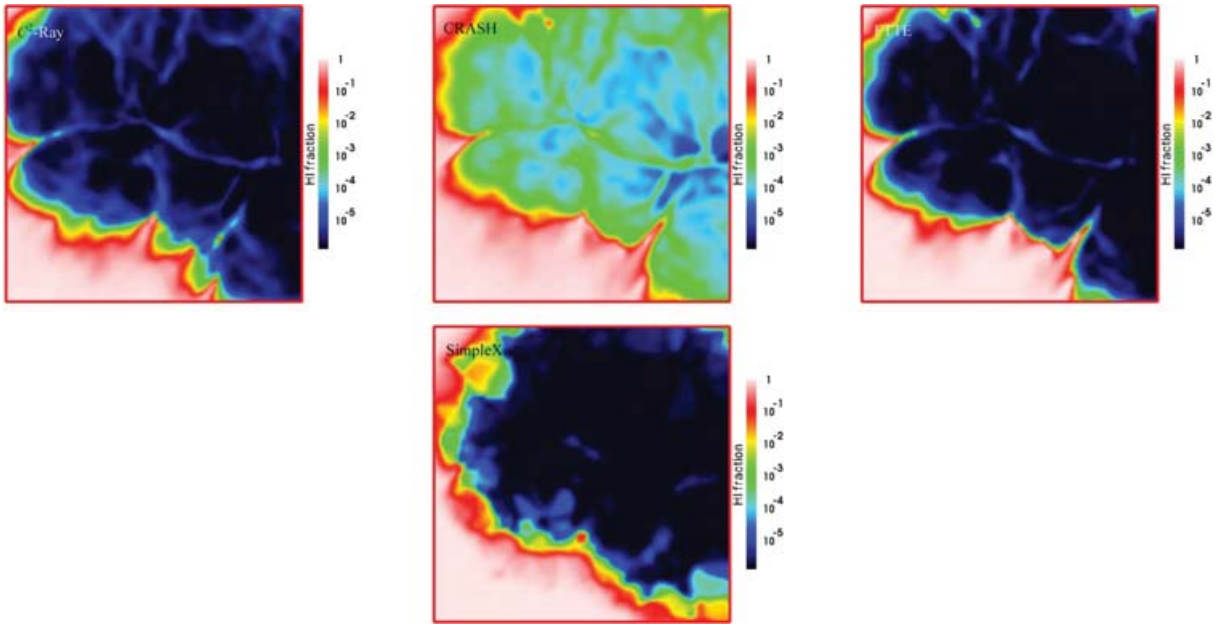

Figure 33. Test 4 (reionization of a cosmological density field): images of the H I fraction, cut through the simulation volume at coordinate $z = z_{\rm box}/2$ and time $t = 0.2$ Myr for C^2-RAY (left-hand panel), CRASH (middle panel), FTTE (right-hand panel) and SIMPLEX (bottom panel). The blackbody spectrum has an effective temperature $T_{\rm eff} = 10^5$ K.

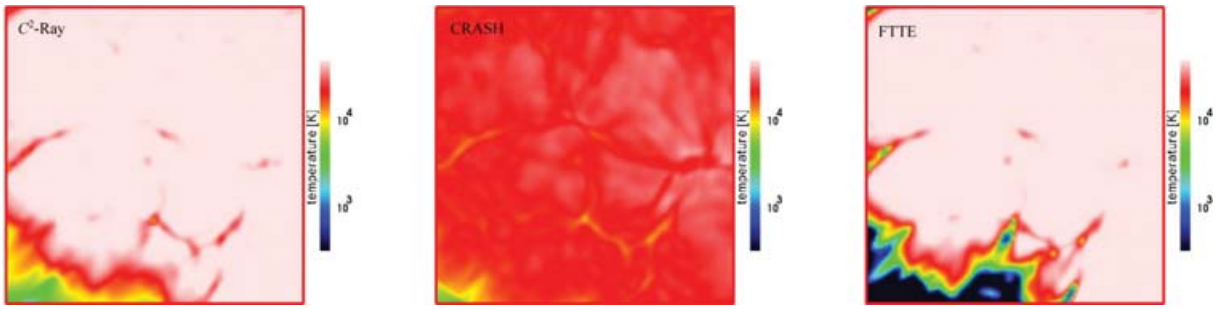

Figure 34. Test 4 (reionization of a cosmological density field): images of the temperature, cut through the simulation volume at coordinate $z = z_{\rm box}/2$ and time $t = 0.2$ Myr for C^2-RAY (left-hand panel), CRASH (middle panel) and FTTE (right-hand panel). The blackbody spectrum has an effective temperature $T_{\rm eff} = 10^5$ K.

their performance on realistic problems, within given convergence criteria.

The differences in computational efficiency among the cosmological RT codes would become even more important when these are directly coupled to gasdynamics and N-body dynamics. All tests in the current paper assume a static density field and no dynamics except for the propagation of I-fronts. We are planning to present a further set of comparison tests which would include

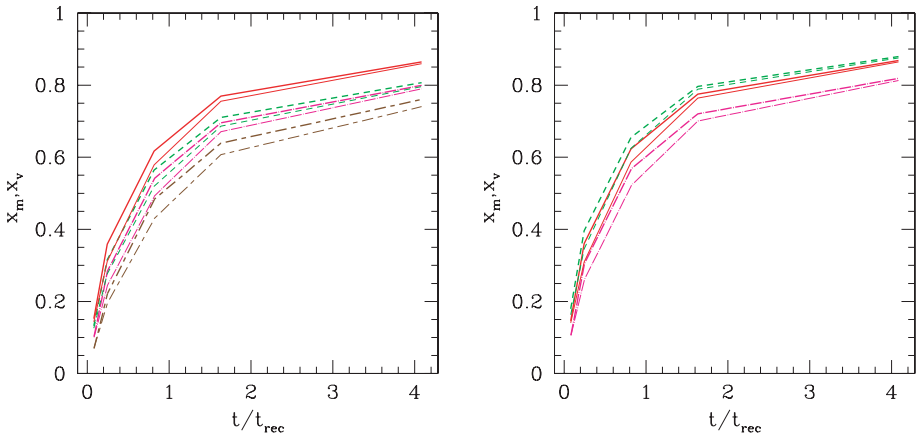

Figure 35. Test 4 (reionization of a cosmological density field): the evolution of the volume- and mass-weighted ionized fractions, x_v (thin lines) and x_m (thick lines), for a blackbody source spectra with $T_{\rm eff} = 10^5$ K (left-hand panel) and $T_{\rm eff} = 3 \times 10^4$ K (right-hand panel).

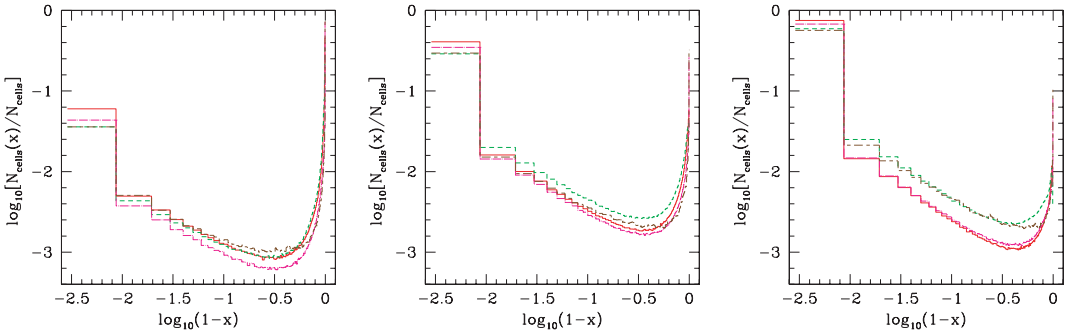

Figure 36. Test 4 (reionization of a cosmological density field): histograms of the neutral fraction at times $t = 0.05$, 0.2 and 0.4 Myr (left to right) for a blackbody source spectrum with $T_{\rm eff} = 10^5$ K.

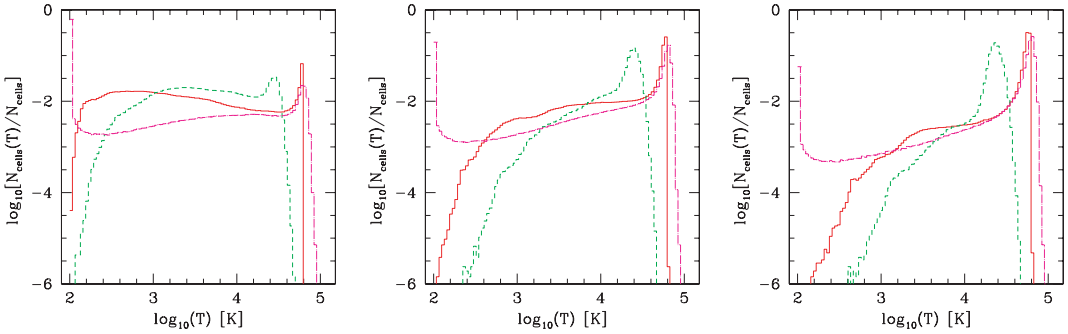

Figure 37. Test 4 (reionization of a cosmological density field): histograms of the temperature at times $t = 0.05$, 0.2 and 0.4 Myr (left to right) for a blackbody source spectrum with $T_{\rm eff} = 10^5$ K.

directly coupled gasdynamics and the corresponding radiative feedback on the gas. Only a subset of the codes is currently coupled to hydrodynamics, and to date only one (OTVET) has run fully self-consistent cosmological simulations including dark matter, gasdynamics and RT. A number of other very important, but also much more computationally challenging physical processes include scattering of radiation, molecular and metal chemistry, and propagation of non-ionizing radiation [far-ultraviolet (FUV), Lyα]. These processes, once they become more widely available in cosmological RT codes, should be considered in future similar code comparison projects.

ACKNOWLEDGMENTS

We are very grateful to the Canadian Institute for Theoretical Astrophysics (CITA) and the Lorentz Center at Leiden University for their hospitality at the two workshops in 2005 which made this project possible, and to NSERC for funding support. We thank Douglas Scott for his careful reading of the manuscript and many useful comments which improved it significantly. This work was partially supported by NASA Astrophysical Theory Program grants NAG5-10825 and NNG04GI77G to PRS. GM acknowledges the support from the Royal Netherlands Academy of Art and Sciences. MAA is

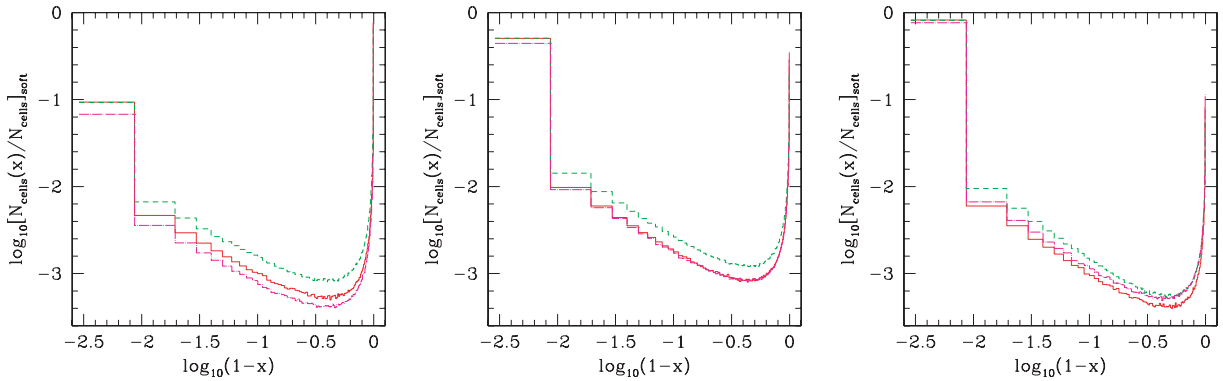

Figure 38. Test 4 (reionization of a cosmological density field): histograms of the ionized fraction at times $t = 0.05$, 0.2 and 0.4 Myr (left to right) for a blackbody source spectrum with $T_{\rm eff} = 3 \times 10^4$ K.

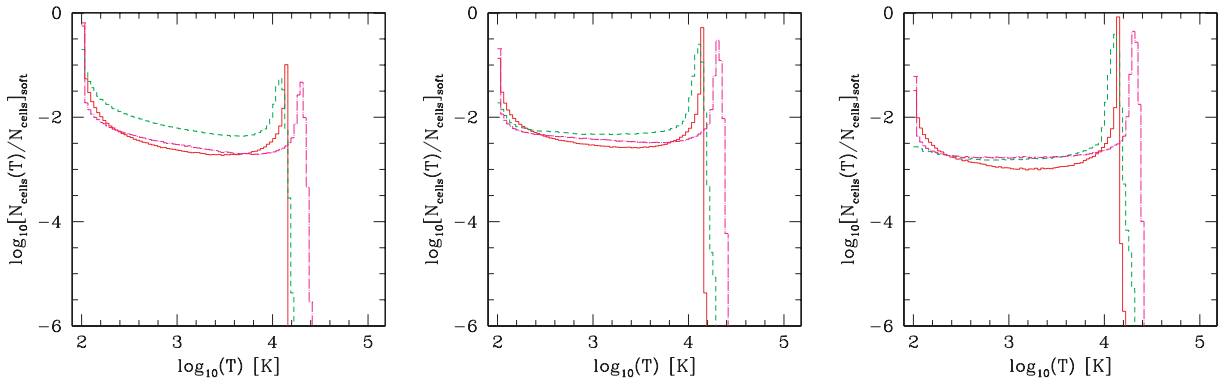

Figure 39. Test 4 (reionization of a cosmological density field): histograms of the temperature at times $t = 0.05$, 0.2 and 0.4 Myr for a blackbody source spectrum with $T_{\rm eff} = 3 \times 10^4$ K.

grateful for the support of a DOE Computational Science Graduate Fellowship. The software used in this work was in part developed by the DOE-supported ASC/Alliance Center for Astrophysical Thermonuclear Flashes at the University of Chicago. DJW was funded in part by the US Department of Energy through its contract W-7405-ENG-36 with the Los Alamos National Laboratory.

REFERENCES

Abel T., Wandelt B. D., 2002, MNRAS, 330, L53
Abel T., Anninos P., Zhang Y., Norman M. L., 1997, New Astron., 2, 181
Aggarwal K. M., 1983, MNRAS, 202, 15P
Aldrovandi S. M. V., Pequignot D., 1973, A&A, 25, 137
Alvarez M. A., Bromm V., Shapiro P. R., 2006, ApJ, 639, 621
Anninos P., Zhang Y., Abel T., Norman M. L., 1997, New Astron., 2, 209
Black J. H., 1981, MNRAS, 197, 553
Burgess A., Seaton M. J., 1960, MNRAS, 121, 471
Cen R., 1992, ApJS, 78, 341
Ciardi B., Ferrara A., 2005, Space Sci. Rev., 116, 625
Ciardi B., Ferrara A., Marri S., Raimondo G., 2001, MNRAS, 324, 381
Cox D. P., 1970, PhD thesis, Univ. California, San Diego
Dalgarno A., McCray R. A., 1972, ARA&A, 10, 375
Frank A., Mellema G., 1994, A&A, 289, 937
Frenk C. S. et al., 1999, ApJ, 525, 554
Fryxell B. et al., 2000, ApJS, 131, 273
Fukugita M., Kawasaki M., 1994, MNRAS, 269, 563
Galli D., Palla F., 1998, A&A, 335, 403
Gnedin N. Y., Abel T., 2001, New Astron., 6, 437
Górski K. M., Banday A. J., Hivon E., Wandelt B. D., 2002, in Bohlender D. A., Durand D., Handley T. H., eds, ASP Conf. Ser. Vol. 281, Astronomical Data Analysis Software and Systems XI. Astron. Soc. Pac., San Francisco, p. 107
Górski K. M., Hivon E., Banday A. J., Wandelt B. D., Hansen F. K., Reinecke M., Bartelmann M., 2005, ApJ, 622, 759
Haiman Z., Thoul A. A., Loeb A., 1996, ApJ, 464, 523
Heinemann T., Dobler W., Nordlund A., Brandenburg A., 2006, A&A, 448, 731
Hui L., Gnedin N. Y., 1997, MNRAS, 292, 27
Hummer D. G., 1994, MNRAS, 268, 109
Hummer D. G., Storey P. J., 1998, MNRAS, 297, 1073
Iliev I. T., Shapiro P. R., Raga A. C., 2005, MNRAS, 361, 405
Iliev I. T., Hirashita H., Ferrara A., 2006a, MNRAS, 368, 1885
Iliev I. T., Mellema G., Pen U. L., Merz H., Shapiro P. R., Alvarez M. A., 2006b, MNRAS, 369, 1625
Janev R. K., Langer W. D., Evans K., 1987, Springer Series on Atoms and Plasmas: Elementary Processes in Hydrogen–Helium Plasmas – Cross Sections and Reaction Rate Coefficients. Springer-Verlag, Berlin
Lang K. R., 1974, Astrophysical Formulae: A Compendium for the Physicist and Astrophysicist. Springer-Verlag, New York, p. 760
Maselli A., Ferrara A., 2005, MNRAS, 364, 1429
Maselli A., Ferrara A., Ciardi B., 2003, MNRAS, 345, 379
Mellema G., Lundqvist P., 2002, A&A, 394, 901
Mellema G., Raga A. C., Canto J., Lundqvist P., Balick B., Steffen W., Noriega-Crespo A., 1998, A&A, 331, 335
Mellema G., Arthur S. J., Henney W. J., Iliev I. T., Shapiro P. R., 2005, ApJ, in press (astro-ph/0512554)
Mellema G., Iliev I. T., Alvarez M. A., Shapiro P. R., 2006a, New Astron., 11, 374
Mellema G., Iliev I. T., Pen U. L., Shapiro P. R., 2006b, MNRAS submitted (astro-ph/0603518)
Nakamoto T., Umemura M., Susa H., 2001, MNRAS, 321, 593

Osterbrock D. E., 1974, Astrophysics of Gaseous Nebulae. Freeman & Co., San Francisco, p. 263
Osterbrock D. E., 1989, Astrophysics of Gaseous Nebulae and Active Galactic Nuclei. University Science Books, Mill Valley, CA, p. 422
Peebles P. J. E., 1971, Princeton Series in Physics: Physical Cosmology. Princeton Univ. Press, Princeton, NJ
Peebles P. J. E., 1993, Princeton Series in Physics: Principles of Physical Cosmology. Princeton Univ. Press, Princeton, NJ
Raga A. C., Mellema G., Lundqvist P., 1997, ApJS, 109, 517
Raga A. C., Mellema G., Arthur S. J., Binette L., Ferruit P., Steffen W., 1999, Rev. Mex. Astron. Astrofis., 35, 123
Razoumov A. O., Cardall C. Y., 2005, MNRAS, 362, 1413
Razoumov A. O., Norman M. L., Abel T., Scott D., 2002, ApJ, 572, 695
Rijkhorst E.-J., 2005, PhD thesis, Univ. Leiden, Netherlands
Rijkhorst E.-J., Plewa T., Dubey A., Mellema G. 2006, A&A, 452, 907
Ritzerveld J., 2005, A&A, 439, L23
Ritzerveld J., Icke V., Rijkhorst E.-J., 2003, preprint (astro-ph/0312301)
Ryu D., Ostriker J. P., Kang H., Cen R., 1993, ApJ, 414, 1
Shapiro P. R., Kang H., 1987, ApJ, 318, 32
Shapiro P. R., Iliev I. T., Raga A. C., 2004, MNRAS, 348, 753
Shapiro P. R., Iliev I. T., Alvarez M. A., Scannapieco E., 2005, ApJ, prepress (astro-ph/0507677)
Sherman R. D., 1979, ApJ, 232, 1
Spitzer L., 1978, Physical Processes in the Interstellar Medium. Wiley, New York
Springel V., 2005, MNRAS, 364, 1105
Steinmetz M., Mueller E., 1993, A&A, 268, 391
Stone J. M., Norman M. L., 1992, ApJS, 80, 753
Strömgren B., 1939, ApJ, 89, 526
Susa H., 2006, PASJ, 58, 445
Susa H., Kitayama T., 2000, MNRAS, 317, 175
Susa H., Umemura M., 2004, ApJ, 600, 1
Tenorio-Tagle G., Bodenheimer P., Lin D. N. C., Noriega-Crespo A., 1986, MNRAS, 221, 635
Thacker R. J., Tittley E. R., Pearce F. R., Couchman H. M. P., Thomas P. A., 2000, MNRAS, 319, 619
Tucker W. H., Gould R. J., 1966, ApJ, 144, 244
Umemura M., 1993, ApJ, 406, 361
Verner D. A., Ferland G. J., Korista K. T., Yakovlev D. G., 1996, ApJ, 465, 487
Voronov G. S., 1997, At. Data Nucl. Data Tables, 65, 1
Whalen D., Norman M. L., 2006, ApJS, 162, 281

This paper has been typeset from a TEX/LATEX file prepared by the author.